Spring 5-15-2019

Microsphere-based Disordered Photonic Structures: Control of Randomness in Langmuir-Blodgett Assembly and Radiative Cooling Applications

Sarun Atiganyanun

Sarun Atiganyanun
Candidate

Nanoscience and Microsystem Engineering
Department

This dissertation is approved, and it is acceptable in quality and form for publication:

Approved by the Dissertation Committee:

Sang Eon Han, Chairperson

Sang M. Han

Andrew Shreve

Terefe Habteyes

MICROSPHERE-BASED DISORDERED PHOTONIC STRUCTURES: CONTROL OF RANDOMNESS IN LANGMUIR-BLODGETT ASSEMBLY AND RADIATIVE COOLING APPLICATIONS

BY

SARUN ATIGANYANUN

B.S., Applied Physics, California Institute of Technology, 2013

M.S., Nanoscience and Microsystem Engineering, University of New Mexico, 2018

DISSERTATION

Submitted in Partial Fulfillment of the

Requirement for the Degree of

Doctor of Philosophy

Nanoscience and Microsystem Engineering

The University of New Mexico

Albuquerque, New Mexico

May, 2019

Dedication

This work is dedicated to my mother, Pratuangsri Likhitsan and my father, Sompong Atiganyanun. It is also dedicated to my grandmother, Kalang Sae Wang, and my brother, Pitchaya Atiganyanun.

Acknowledgement

I would like to express my deepest appreciation to my advisors, Professor Sang Eon Han and Professor Sang M. Han, for offering me a chance to join in their research groups to conduct research. Their guidance and encouragement have helped me work through difficulty in the research. Their expertise and insight are invaluable and help me grow as a researcher.

I would like to thank Professor Andrew Shreve for allowing me to access his equipment for my research and for being a part of my committee.

I would like to thank Professor Terefe Habteyes for being a part of my committee and for his valuable comments given during my comprehensive exam regarding this work.

I would like to thank Dr. Ying-Bing Jiang for his help with characterization of my samples.

I would like to thank my group members and ex-group members, Mi Zhou, Dr. John Plumley, Dr. Swapnadip Ghosh, Dr. Seung Ho Lee, Dr. Omar Abudayyeh, Dr. Seok Jun Han, Kevin Hsu, Joseph Aldren, Jacob Cytrynbaum, Emma Clink, and all other group members for their inputs and stimulating discussion. It has been a rewarding experience working in a group with a great spirit of teamwork.

I would like to acknowledge generous financial support from the National Science Foundation and Air Force Research Laboratory.

Finally, I would like to thank my mother Pratuangsri Likhitsan and my father Sompong Atiganyanun, my grand mother Kalang Sae Wang, and my brother Pitchaya Atiganyanun for their love and supports.

MICROSPHERE-BASED DISORDERED PHOTONIC STRUCTURES: CONTROL OF RANDOMNESS IN LANGMUIR-BLODGETT ASSEMBLY AND RADIATIVE COOLING APPLICATIONS.

by

Sarun Atiganyanun

B.S., Applied Physics, California Institute of Technology, 2013
M.S., Nanoscience and Microsystem Engineering, University of New Mexico, 2018
Ph.D., Nanoscience and Microsystem Engineering, University of New Mexico, 2019

ABSTRACT

Many biological photonic structures in nature exhibit a significant degree of disorder within their periodic framework that enhances their optical properties. However, how such disorder contributes to the unique photonic characteristics is not yet fully understood. To facilitate studies on this topic, we investigated self-assembly of microspheres as a method to controllably introduce randomness to photonic structures. Specifically, we examined Langmuir-Blodgett assembly, a layer-by-layer fabrication technique. We developed and experimentally verified a model for the process and determined a condition of surface pressure and substrate pulling speed that corresponds to a maximum structural order in a layer. Along the trajectory described by this condition, disorder can be controllably introduced by increasing the pulling speed. Our model also

describes a condition for maximum structural order for multilayer assembly: as the number of layers increases, the surface pressure should also increase at a fixed pulling speed. Overall, we have demonstrated that by carefully choosing assembly parameters along the optimal trajectory, disorders within Langmuir-Blodgett films can be systematically introduced.

To further demonstrate usefulness of disordered photonic structures fabricated from self-assembly methods, we investigated radiative cooling performance of microsphere-based disordered materials under direct sunlight. Radiative cooling is a process in which an object passively loses heat via radiation and thus has a potential to reduce consumption of electricity used for thermal management. Toward a goal of making radiative cooling technology more accessible, we investigated two scalable, and inexpensive methods for fabricating microsphere-based structures that can achieve efficient radiation cooling. Specifically, colloidal sedimentation method and spray coating were employed to create coatings that consist of randomly arranged microspheres. With a systematic study of light scattering in microsphere-based disordered media, we showed how structural parameters influence radiative cooling performance. By combining this understanding with the two facile fabrication methods, we demonstrated that black substrates coated with our microsphere-based materials achieved substantial cooling below ambient temperature even under direct sunlight exposure. Our coatings also outperformed commercially available paints designed for daytime cooling, without use of sophisticated fabrication process or expensive materials. We demonstrated further that cooling capability of our microsphere-based structures was improved by using hollow microspheres instead of solid particles and that mechanical

durability was enhanced when the hollow microspheres were embedded in a silicone matrix. Overall, this work provides a path toward wider applications of radiative cooling achieved by microsphere-based disordered systems.

TABLE OF CONTENTS

LIST OF FIGURES

Chapter 1: Introduction

1.1 Random photonics in nature and its importance

Photonic crystals are synthetic materials that are periodic on the optical wavelength scale. They strongly interact with light and demonstrate unique optical phenomena, such as photonic bandgap [1–5] and absorption or emission enhancement. [6–12] Light of frequency within a photonic bandgap can be localized or guided through defects in photonic crystals. [4,13–18] However, light outside the bandgap can be randomly scattered by non-periodic structural defects and disorders. This random optical scattering in photonic crystals is generally considered a problem or an error in fabrication process.

Nevertheless, various photonic structures found in animals and plants possess a significant degree of disorders in the periodic structures, which enhances their optical properties. [19–24] For examples, butterfly (*Morpho rhetenor*) wings and leaves of many plants of genus *Selaginella* exhibit bright iridescent blue color generated from their imperfect periodic structures. [25–27] In contrast, feathers from five species of bird-of-paradise (*Aves*: *Paradisaeidae*) achieve absorptance up to 99.95% of incident light by employing vertically tilted barbules arranged in a disordered fashion to increase the number of absorption events that occur within the structures. [28] The fact that disorder in these biological photonic structures gives rise to beneficial optical properties suggests that such disorders should not be readily considered an error as traditionally thought.

Notably, the degree of disorder in the biological structures is much greater than that in typical fabricated photonic crystals. This level of imperfection observed in nature

suggests that a certain degree of structural randomness, a result of millions of years of evolution, is favorable or necessary for the best optical performance to ensure their survival. Understanding the underlying physics of these optical phenomena and exploring fabrication techniques for mimicking these optical structures may give us guidance to novel optical properties and significant improvement in optical performance. Indeed, the usefulness of structural randomness has been explored and incorporated into some fabricated systems. For instance, introducing some structural disorder into solar photovoltaics can improve light-trapping efficiency over both periodic and highly random structures. [29–31] Because of the potential advantages in introducing disorder in photonic structures and fascinating and rich physics behind the phenomena, the field of disordered photonics has gained significant momentum over the past decade.

1.2 Current works in introducing degree of randomness

Methods for introducing disorder into photonic structures or fabricating such media with controllable degree of randomness are essential for understanding and eventually exploiting the useful photonic properties associated with the introduction of disorder. Nanofabrication continues to be a powerful and precise technique for this purpose. [32–36] For example, a single defect can be introduced in a two-dimensional photonic crystal during electron-beam lithography process to create a cavity that lases in a defect mode. [14] While nanofabrication remains a useful set of techniques, its high cost can be often prohibitive to introducing randomness in photonic structures for wider-scale applications.

On the other hand, self-assembly of colloidal particles, while having less precision, provides simple, scalable, and less expensive techniques for fabrication of photonic crystals. If tailored for creating a highly ordered structures, this method can achieve a very low defect density (≤1 point defect per 1000 unit cells) over centimeter-scale samples. [3,36,37] The convenience and long-range structural order resulting from self-assembly have contributed to advances in experimental research in photonic crystals. [39] Popular self-assembly methods include convective assembly of vertical substrates, [3,39,40] slow sedimentation of colloidal microspheres, [5,41] and Langmuir-Blodgett (LB) assembly. [42–45] These works exploit the nature of uniformity in interaction of colloidal particles to create ordered structures.

Furthermore, self-assembly techniques are also capable of creating highly disordered photonic structures by introducing instability in the colloidal interaction. [46–48] For example, disruption in the balance between electrostatic potential and van der Waals potential in colloids can lead to random agglomerations of the particles, which once settled form a highly disordered film. [46] Forcing sedimentation of colloidal particles by introducing additional attractive force between colloids and a substrate can create a highly uniform film comprised of disordered arrangement of the particles. [47]

However, the gap between the two opposite capabilities of self-assembly remains: to introduce controllable randomness in photonic structures, especially periodic ones, in a systematic manner. To address this gap, these self-assembly techniques must be investigated further. In this dissertation, we choose to study the Langmuir-Blodgett (LB) assembly of microspheres. Specifically, we aim to establish how LB process parameters can be manipulated to controllably introduce randomness. One important reason that LB

assembly is chosen for this study is that it is a layer-by-layer process. By controllably introducing randomness in each layer during deposition, systematic control of disorder in LB assembled films can be achieved. Generally, creating highly uniform and ordered films is an ultimate goal of LB assembly. Therefore, by tailoring the LB process for controllable introduction of disorder, we aim to expand the capabilities of LB assembly.

1.3 Radiative cooling

One important application of disordered photonic materials is in efficient management of solar energy. While the use of solar radiation for heating has been extensively explored [49,50], the possibility of cooling by preventing sunlight absorption and maximizing thermal radiation in mid-infrared spectrum, namely radiative cooling, is considered less developed. Nevertheless, because this radiative cooling mechanism does not require electricity to function, this technology is an efficient thermal management method that could reduce electricity consumption. According to federal surveyed data, [51,52] the number of surveyed U.S. households that are equipped with air conditioners increased from 83 percent in 2009 to 87 percent in 2015. Additionally, the electricity used for cooling in the U.S. is ~15% of the total energy consumption in households. [53] Because of this increasing trend in energy consumption for household cooling, the cost saving that can be achieved by incorporating radiative cooling technology can be substantial. Usage of this technology in other applications, such as automobile, transportation, and water collection, can reduce electricity consumption even further.

Researchers have demonstrated strong performance of radiative cooling back in 1960s and achieved cooling almost 40°C below ambient temperature at night. [54–56] This subject has become of interest again with a seminal work in 2014 that demonstrated radiative cooling of an object by 5°C under direct sunlight. [57] The cooling structure in this work is a complex nanostructure, comprised of seven alternating thin layers of hafnium dioxide and silicon dioxide on top of a thin silver layer, which are all deposited on a silicon wafer via electron beam evaporation. In tandem with the solar-reflective silver layer, the dielectric layers reflect incident solar radiation in a manner similar to a Bragg reflector. The mid-IR emission in the structure mainly occurs in the first few dielectric layers due to intrinsically high mid-IR emission of silicon dioxide.

This strong solar rejection can also be also achieved with reflective metal film alone. [58–60] For example, Zhai et al. [59] creates flexible films comprised of polymer-based metamaterial backed by a silver layer that is responsible for rejection of incident solar radiation. While the films can be fabricated with a high throughput roll-to-roll process, the usage of silver has a significant impact on the cost of fabrication. Therefore, because both complex microstructure and metal films are expensive to fabricate, photonic structures designed for radiative cooling at a wider scale must be fabricated in less expensive and more scalable ways.

In this dissertation, we investigate fabrication and use of disordered microsphere-based coatings to achieve strong radiative cooling performance without using any metals. Microspheres are abundant and can be mass-manufactured at an economical cost. Coatings comprised of randomly arranged microspheres could scatter incident light many times due to their disordered nature. If the light scattering properties are systematically

studied and optimized, strong rejection of incident solar radiation could be achieved. Heat radiated in the mid-IR spectrum can also be improved by judicious selection of material that comprises the microspheres. We will also explore simple and less expensive fabrication methods to create such disordered microsphere-based structures. Cooling capabilities of the coatings will be compared to the coatings in the previous works and commercial solar reflective products. Our goal is to ultimately provide a path for radiative cooling to become a more mainstream technology for solar energy management.

1.4 Organization of the dissertation

Chapter 1 introduces the phenomenon of optical scattering in photonic media that incorporate a degree of disorder and its importance in nature. Methods to fabricate such media, particularly those made of microspheres, are mentioned. Langmuir-Blodgett assembly is proposed as a self-assembly method for introducing randomness into periodic structures. Radiative cooling is introduced as one significant application of such media. We justify our plan for creating disordered microsphere-based coating to achieve strong radiative cooling performance while keeping the cost of fabrication economical.

Chapter 2 explores the Langmuir-Blodgett technique as a facile method of introducing a degree of randomness into photonic crystals. Although the technique is commonly used to create highly ordered structures, this work will show that by systematically and carefully detuning assembly parameters away from optimal ordering conditions, controllable degrees of randomness can be induced into otherwise ordered structures. This chapter investigates the dynamics of LB assembly via material transport

modeling and characterization techniques including optical scattering measurement and scanning electron microscopy.

In chapter 3 radiative cooling properties of microsphere-based disordered structures are investigated. Two approaches to fabricate such structures, colloidal sedimentation and spray coating, are described. Diffusion theory of light transport in random media is invoked to introduce the concept of transport mean free path, which is related to scatter strength. A calculation is developed to predict how this value depends on structural parameters. Characterization of the optical properties of the structures via a spectrophotometer and an integrating sphere is employed to measure the transport mean free path, which is then compared to the theoretical results. The radiative cooling properties of the samples are tested in an outdoor environment and are compared with those of solar-rejection commercial paints.

Chapter 4 further describes studies of radiative cooling with disordered structures comprised of hollow polymer microspheres. Based from the work described in chapter 3, we speculate that the hollow microspheres can improve solar scattering performance. The spray coating method is employed to fabricate the structures. The transport mean free path of the disordered hollow sphere-based structures is characterized and compared to that of the silica microsphere-based structures. Emissivity spectrum is also measured to predict radiative cooling performance of the structures. Radiative cooling performance of the media is also tested in an outdoor setup. We further improve both cooling performance and mechanical stability of hollow microspheres-based structures by embedding the microbubbles into silicone matrix.

Chapter 5 discusses conclusions and future directions of work described in this thesis.

Chapter 2: Control of Randomness in Langmuir-Blodgett Films

*Reproduced in part with permission from S. Atiganyanun, M. Zhou, O. K. Abudayyeh, S. M. Han, and S. E. Han, Langmuir **33**, 13783 (2017). DOI: 10.1021/acs.langmuir.7b03060.

2.1 Langmuir-Blodgett assembly overview

Langmuir-Blodgett (LB) process is a self-assembly fabrication method where a layer or layers of particles or molecules are transferred from a horizontal liquid surface onto a vertical substrate in a layer-by-layer process. LB assembly, among other self-assembly methods, has been widely used to create photonic structures. [42–45,61–66] In these LB works, it is desirable to achieve long-range order in the fabricated photonic crystals. Nonetheless, defects and disorder still remain in the structures. In our work, we approach the LB assembly from another perspective. Rather than considering defects as inherently undesirable, we seek to controllably introduce randomness into periodic structures in a systematic manner. Specifically, we aim to establish how LB process parameters, i.e. surface pressure, pulling speed, and number of layer, can be manipulated to controllably introduce randomness.

In previous studies on microsphere LB assembly, much attention has been given to the surface pressure in the liquid surface. [61,63,65] A wide range of surface pressures (0 and ~25 mN/m) has been claimed to achieve high degree of order. [44,45,61,63,65,66] In this work, we demonstrate that the degree of randomness in photonic crystals can be controlled in LB assembly by manipulating the substrate pulling speed in addition to the

surface pressure. We also modify a model proposed by Dimitrov and Nagayama [67] to describe the monolayer LB assembly and determine a condition that interrelates surface pressure and substrate pulling speed to achieve maximum structural order. Our experiment confirms that such a condition exists. Further, we find that increasing the pulling speed, while this condition is met, gradually increases randomness. We also investigate how the condition for maximum order changes as the number of layers increases. We show that, at a fixed pulling speed, to maintain maximum order, the surface pressure must increase when the number of layers increases.

2.2 Key concept and process in Langmuir-Blodgett assembly

The process of fabrication in LB assembly is described in Fig. 2.1 below. A Langmuir Blodgett trough, generally made of PTFE or other low surface energy material, is first filled up with a liquid, called subphase. A common choice for a subphase is deionized water. Particles and molecules are dispersed on the subphase (Fig. 2.1(1)). Due to particles dispersed on the subphase, there is a change in surface tension. Decrease in surface tension is assigned as surface pressure (π) in LB assembly:

$$\pi = \gamma_0 - \gamma \,, \tag{2-1}$$

where γ_0 and γ are surface tension of a pure subphase and the subphase with dispersed particles respectively. There are a number of factors that can affect the behavior of the surface pressure. For example, the factors are surface energy of particles and a subphase, the interaction between particles and subphase, and number density of particles. In

practice, the number density of particles on a subphase is set to be at a lower value before compression and thus the surface tension is approximately zero after particle dispersion.

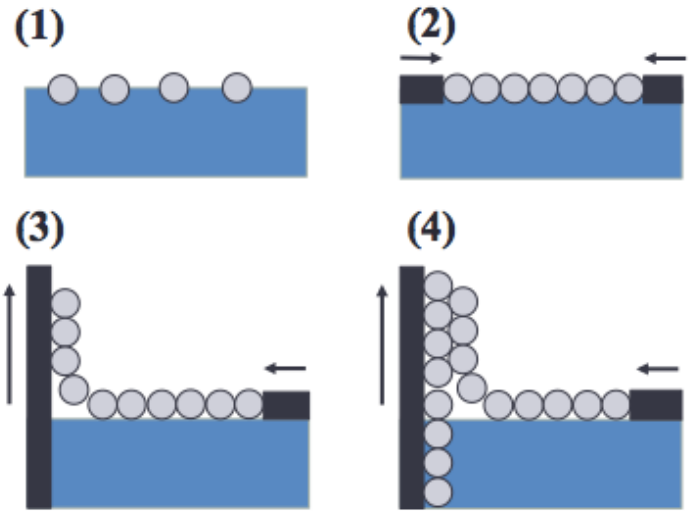

Figure 2.1 Diagram of LB assembly process.

In the next step (Fig. 2.1(2)), barriers gradually compress the dispersed particles by reducing an area that contains the particles. The goal of this compression step is to induce a formation of a monolayer of the particles on the subphase. Arrangement of the particles on this monolayer depends on many factors such as the degree of compression and particle surface energy. At the beginning of compression, particles are still far apart from one another and thus the surface pressure remains at zero. As the compression continues and the area per particle decreases, the particles enter a phase where they begin interacting and lead to an increase in surface pressure. There can also be more than one phase where surface pressure changes at different rates. This dependence of surface pressure on area per particle at a fixed temperature is called a Langmuir-Blodgett isotherm, which provides a clue into understanding the interaction between particles. In

other words, LB isotherm is equivalent to a pressure-volume isotherm in thermodynamic studies of gases.

Once a monolayer is compressed as desired, particles can be simply transferred to a substrate by vertically submerging it into the subphase and withdrawing it in an opposite direction (Fig. 2.1(3)). Depending on the nature of the particles and the substrate, particles can be deposited during the submerging, the withdrawal, or both. This process can be repeated to transfer multiple monolayers (Fig. 2.1(4)). At each transfer, a surface pressure is commonly maintained at a constant value. However, as the number of particles decreases due to them being deposited onto the substrate, barrier compression must accompany the deposition to maintain a constant value of area per particle and thus surface pressure.

2.3 Experimental design and details

The crux of this work is to explore the assembly parameter space and investigate how it affects disorder of LB films. Therefore LB assembled samples are carefully created for many conditions and then are characterized by light diffraction to extract a parameter that represents degree of disorder. Due to the sensitive nature of LB assembly, prior preparations before the actual assembly are very important and should be followed closely. Studying of an LB isotherm is also recommended before fabricating any samples, since the isotherm provides a clue into inter-particle interaction and suggests appropriate values of the assembly parameters.

i) Microsphere Solution Preparation

Non-functionalized silica microspheres were purchased from Polysciences (Cat. No. 24326-15). The microspheres were delivered in an aqueous solution, and the polydispersity of this batch was 15 % based on the vendor-provided product information as well as our electron micrograph images. The surface of silica microspheres (~900 nm in diameter) was functionalized with allyltrimethoxysilane. This functionalization is essential because it is to provide a balance between hydrophobicity and hydrophilicity. [64] The attached allyl groups introduce hydrophobicity to the microsphere surface, prevent the aggregation of microspheres in solution, and allow them to remain near the surface of the water. [65] On the contrary, silicate bonds, intrinsic to the silica microspheres, provide enough counterbalancing hydrophilicity such that the microspheres are almost fully immersed just below the water surface in the LB trough (see Appendix A). This hydrophilicity also promotes adhesion to hydrophilic silicon substrates used in this work. However, excessive allyl functionalization can lead to large voids in final products.

The method for the functionalization is as follows. 500 μL of 10 wt% microsphere solution was first centrifuged, so that the microspheres sediment to the bottom. Then, the water was decanted, and the microspheres were dispersed in ethanol. Ethanol helps solvate allyltrimethoxysilane and promotes its reaction with the silicate groups. The solution was sonicated for 45 minutes, and 10 μL of allyltrimethoxysilane was added to the solution. The solution was then further sonicated for 2 hours. It should be noted that, for consistency in results, the water in the sonicator should be kept at the room temperature. After sonication, the microspheres were washed in ethanol 3 times to remove residual allyltrimethoxysilane from the solution. The washing was done with

multiple cycles of centrifugation, extracting solvent, re-introducing ethanol, and sonication. Sonication should not be done for too long (> 5 minutes) as this may further affect the functionalization.

Lastly, the microspheres were dispersed in 500 μL of chloroform. Sonication can be used to promote dispersion. Based on the microsphere density of 2.0 g/cm^3 provided by the manufacturer, the total number of microspheres in the chloroform solution (50 μL) was estimated to be 6.9×10^{10}. This final solution should be used in the assembly as soon as it is prepared since agglomeration can occur in the solution if it is left for too long. Another caution is that plastic centrifuge tubes cannot be used to contain the chloroform solution since chloroform reacts with the tubes and creates contaminants that significantly affect the LB assembly.

ii) Substrate Preparation

Substrates (3 *cm* × 1 *cm*) diced from *n*-doped (100) silicon wafers with a resistivity greater than 100 Ω-cm were used for LB assembly. A substrate was first washed in deionized water and then treated for 3 minutes in a Piranha solution, which consisted of 125 mL of 96 wt% sulfuric acid and 75 mL of 30 wt% hydrogen peroxide. The substrate was washed again in deionized water and then cleaned for 2.5 minutes with a buffered oxide etchant, a 20:1 volume mixture of 40 wt% ammonium fluoride and 49 wt% hydrofluoric acid. The substrate was washed again in water and treated in the Piranha solution for 3 minutes, so that the silicon surface was oxidized and made hydrophilic. Finally, one last wash with water was done. Substrates prepared this way can be stored in an ambient environment up to three months before they must be prepared

again. As a result of this preparation, silicon dioxide layer is grown on the substrates, rendering them hydrophilic.

iii) Langmuir Blodgett Isotherm Measurement

The LB instrument is KSV NIMA 1212D1 from Nima Technology. The LB trough was first cleaned with deionized water and chloroform. Then the trough was filled up with deionized water, which acted as a subphase. The height of the water should be slightly above the trough's perimeter barrier to facilitate compression at later stage and avoid water overflowing during the compression. A filter paper was used as a Wilhelmy plate to measure the surface pressure. For the first time usage, the surface pressure measurement system should be calibrated, such as by setting the surface pressure of pure D.I. water to 0 mN/m at 25 °C (since pure D.I. water was used as both reference and subphase). It is advised to check the purity of the water by compressing with two barriers of 20 cm in width and recording the surface pressure until the area between the two barriers is less than ~100 cm^2. If the surface pressure does not rise above 0.5 mN/m at that point, then the water is considered clean enough for this experiment.

The microsphere solution in chloroform was then carefully dispersed by a micropipette onto the subphase surface to form a monolayer of microspheres. Significant care should be taken during this dispersion. First, the tip of the micropipette should be a few millimeters or less above the water surface and should not touch it. Second, pushing out the solution should be done very slowly such that a small droplet is formed at the tip and drops down toward the water surface at a minimal initial velocity. These two considerations are to avoid microspheres gaining enough vertical momentum such that they are fully submerged and lost into the water. Solution droplets should be introduced

evenly across the water surface. Once the solution was dispersed, chloroform was let to evaporate for 5 minutes. The waster surface should look clear as if nothing is on the surface. If some material is visible, the surface may be contaminated, and it is advised to redo the experiment.

Subsequently, the monolayer was compressed by two barriers moving toward the trough center line at 0.6325 cm/min, while the area between the two barriers and the surface pressure were recorded. If the monolayer is to be used for assembly, compression should be stopped before the monolayer collapses. The collapse is signified by slowing of the rate of increase in the surface pressure, which follows a sharp increase as the compression progresses. To avoid this collapse, once the pressure starts to rise sharply, the compression should be halted after ~2 seconds of the rise. However, for studying the isotherm behavior, a monolayer can be used solely for this purpose and the collapse can be allowed to occur. In this case, the monolayer cannot be used for assembly.

It is noted that the effective projected area occupied by a single microsphere in the monolayer, which includes part of the spacing between spheres, is slightly greater than the true projected area per microsphere. The projected area is calculated by dividing the area between the trough barriers by the number of microspheres. An LB isotherm is obtained from plotting the effective area per microsphere and the surface pressure.

iv) Langmuir-Blodgett Assembly

The LB assembly was performed at ~22°C and ~20% relative humidity and with limited airflow. A prepared silicon substrate was first submerged into the water before dispersing the solution. The solution was dispersed as described previously. The monolayer of microspheres was compressed by the barriers, so that a target pressure was

reached. The substrate was then pulled out of the LB trough in the vertical direction at a set velocity while the surface pressure was held constant. The control of surface pressure was achieved by a program that adjusted the barrier movement to maintain a targeted pressure. In this work, it was observed that the target pressure should be slightly above the assembly pressure since setting the two pressures to be equal would result in the actual pressure being below the assembly pressure. Gain factor, a value which determines the sensitivity of the program, should be set to ~0.5.

During substrate pulling, a monolayer of microspheres was transferred onto the substrate in a close-packed arrangement. To transfer additional layers, the cycle of dipping and pulling of the sample was repeated. For each additional layer, we varied assembly parameters to determine the optimum pull speed and surface pressure. Once the assembly was complete, the samples were dried in ambient air and characterized for their structural properties.

v) Characterization

The microstructures of the LB-assembled samples were imaged by a scanning electron microscope (FEI Q3D FIB/SEM DualBeam system, ThermoFisher Scientific) at 10 keV electron beam energy. The average domain size of the microsphere crystals was determined from light diffraction experiment. For light diffraction, a He-Ne laser beam at 632.8 nm the sample at normal incidence. Diffraction patterns were projected onto a screen and recorded by a digital camera. The patterns approximately assumed circular symmetry because of the random distribution of the crystalline domain orientations and were fit to an intensity distribution given by

$$I(r) = I_0 e^{-\frac{3\pi G^2}{4\lambda^2}\left[\frac{r\cos\theta}{R}\right]^2}, \tag{2-2}$$

where $I(r)$ is the intensity at a distance r from the pattern center, I_0 is the intensity at the center, λ is the wavelength of the laser, θ is the diffraction polar angle, R is the distance between the beam incident location and the center of the fringe pattern, and G is the representative crystal domain size. G values of samples created with various assembly parameters were extracted from the fitting of Eq. (2-2).

The derivation of the distribution is described here. The light diffraction experiment schematic is shown in Fig. 2.2 below. Light is incident on a sample consisting of crystalline domains that are randomly distributed in orientation. Light is then diffracted from the sample and forms a ring pattern. Because domain orientations are randomly distributed, the intensity of the ring pattern does not have azimuthal dependence. The directions of incident and diffracted light are given by unit vector $\vec{s}_0$ and $\vec{s}$, respectively. We seek to describe the intensity profile as a function of distance from the primary peak in the radial direction of the diffraction ring. To do this, we consider a direction, $\vec{s}'$, that is slightly different from $\vec{s}$. The difference between $\vec{s}'$ and $\vec{s}$, projected onto the plane perpendicular to the diffracted light, is $\overrightarrow{\Delta s}$. First we consider the intensity profile of the pattern from a perfect crystal of a finite size. Then we relate the profile of the crystal to that of the randomly distributed orientation of crystal domains.

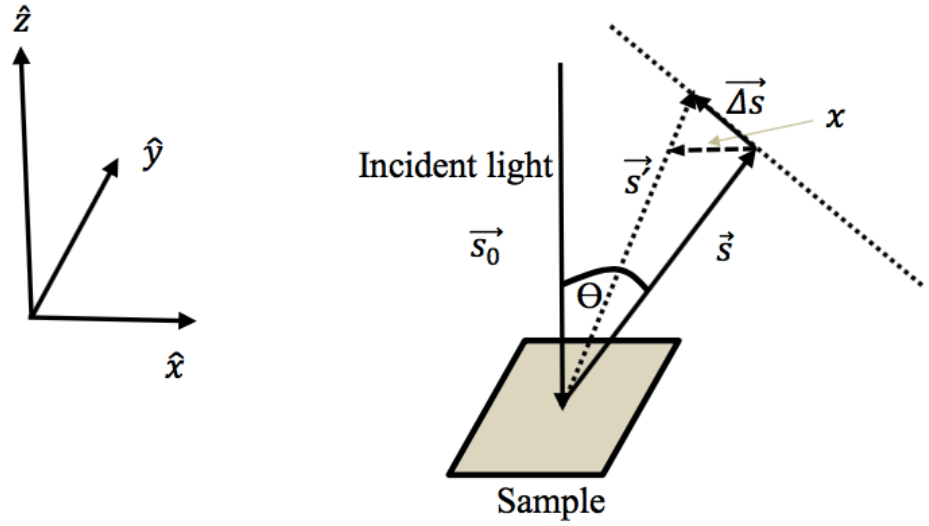

Figure 2.2. Schematic illustration of light diffraction from a 2-dimensional crystal with a disorder. Distance in the figure is normalized by the distance between the beam incident location and the center of the fringe pattern, R.[†]

For a 2-dimentional crystal, the diffraction pattern's intensity profile is given by [68]

$$I = I_0 e^{-\left(\frac{\pi}{\lambda^2}\right)N^2\left\{(\vec{\Delta s}\cdot\vec{a_1})^2+(\vec{\Delta s}\cdot\vec{a_2})^2\right\}}, \tag{2-3}$$

where I is the intensity, I_0 is the intensity at the primary peak, λ is the wavelength of the incident light, N is the number of the unit cells under illumination, and $\vec{a_1}$ and $\vec{a_2}$ are lattice vectors of the crystal. For a hexagonal lattice, the vectors are

$$\vec{a_1} = a\hat{x}$$

$$\vec{a_2} = \frac{1}{2}a\hat{x} + \frac{\sqrt{3}}{2}a\hat{y}$$

where a is the periodicity of the lattice. In a crystal, diffraction occurs in the direction of the reciprocal lattice vectors:

$$\vec{b_1} = -\frac{1}{a}\hat{x} + \frac{1}{\sqrt{3}a}\hat{y}$$

$$\vec{b_2} = \frac{2}{\sqrt{3}a}\hat{y}$$

Now suppose $\vec{\Delta s}$ aligns with $\vec{b_2}$, we can evaluate the factor in the exponent in eq. (2-3) as following

$$(\vec{\Delta s}\cdot\vec{a_1})^2 + (\vec{\Delta s}\cdot\vec{a_2})^2 = \left|\vec{\Delta s}\right|^2\left\{(\hat{y}\cdot a\hat{x})^2 + (\hat{y}\cdot(\frac{1}{2}a\hat{x} + \frac{\sqrt{3}}{2}a\hat{y}))^2\right\} = \frac{3}{4}a^2\left|\vec{\Delta s}\right|^2 . \quad (2\text{-}4)$$

Note that, if we choose $\vec{\Delta s}$ to align with $\vec{b_1}$ instead, the same result is obtained. Therefore, since $\vec{\Delta s}$ must be a linear combination of the two reciprocal lattices, Eq. (2-4) is always satisfied. In our experiment, $\vec{\Delta s}$ is related to the distance *x* indicated in Fig. 2.2 by

$$\left|\vec{\Delta s}\right| = \frac{x\cos\theta}{R} . \quad (2\text{-}5)$$

Applying Eq. (2-4) and (2-5) to Eq. (2-3) and setting the crystal domain size *G* to be equal to *Na*, we get

$$I = I_0 e^{-(\frac{\pi}{\lambda^2})N^2\frac{3}{4}a^2\left|\vec{\Delta s}\right|^2} = I_0 e^{-(\frac{3\pi}{4\lambda^2})G^2\left(\frac{x\cos\theta}{R}\right)^2} . \quad (2\text{-}6)$$

Note that this intensity profile is applicable for any direction that is a linear combination of $\vec{b_1}$ and $\vec{b_2}$. Now if, we consider the case of many crystal domain orientations, the

reciprocal lattice vectors for these domains are still the linear combination of $\vec{b}_1$ and $\vec{b}_2$, since all the domains rest on the same plane. Therefore, the diffraction pattern of randomly oriented crystals in this case can be described by Eq. (2-6).

2.4 Modeling of Langmuir-Blodgett assembly process

Our model is based on the work of Dimitrov and Nagayama [67] and aims to describe the LB process for microsphere assembly. Our model relates the surface pressure and the substrate pulling speed that would induce the maximum structural order, i.e. highest *G* values. Figure 2.3 shows the schematic of the LB assembly process where water is the subphase. This model assumes that the top of the microspheres is close to the water surface. This behavior happens when the microsphere surface has appropriate balance between hydrophobicity and hydrophilicity. The assumption is approximately valid in our experiment as verified in the appendix A. In the model, the submerged microspheres with a diameter *d* at the water surface are pushed laterally toward a vertical substrate by two barriers on either side of the substrate. Each barrier is moving horizontally with a speed of v_b, and the substrate is vertically pulled out of the water with a speed of v_c. As the area between the two barriers close, packing of microspheres becomes denser, causing increase in the surface pressure, π. The assembly occurs when the substrate is being pulled out while the surface pressure is maintained at a constant value. During the pull, the microspheres on the liquid surface are transferred onto the substrate. Water evaporates from the meniscus over the vertical layer exposed to the ambient air at a volumetric flow rate per unit substrate width, J_{evap} (cm^3/cm-sec). J_{evap} is approximately a constant determined by the humidity of the ambient air. [67] The

thickness of the water film at the lowest point of the assembled microsphere crystal is defined as h_f.

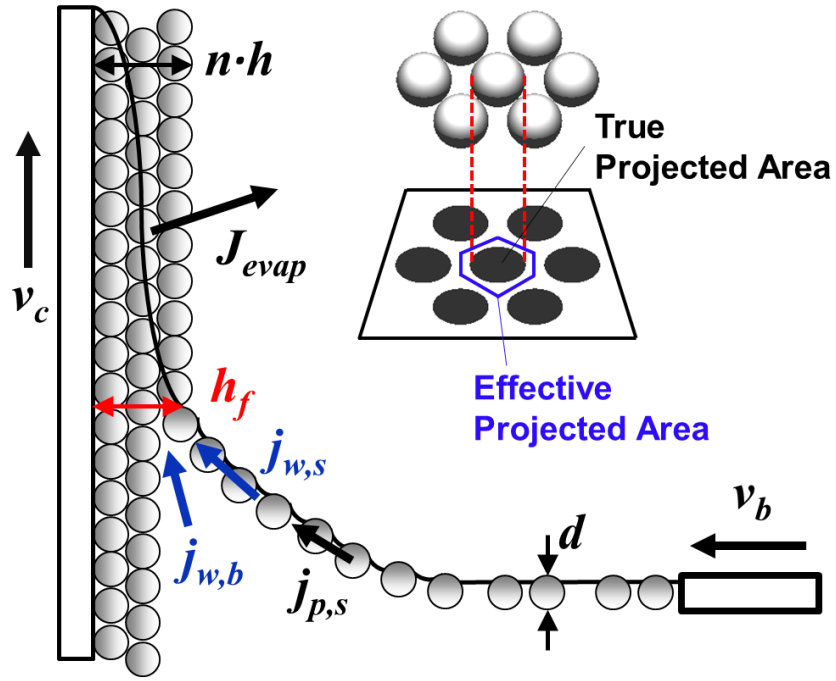

Figure 2.3. Schematic illustration of the LB assembly of microspheres and the definition of the assembly parameters. Inset illustrates the true projected area and the effective projected area.[†]

Multilayer structures can be fabricated by repeating the transfer process. In our case, a layer is deposited only in each upward movement. In this layer-by-layer approach, randomness is naturally introduced in each layer, and our goal is to control the overall degree of randomness via adjusting assembly parameters. The thickness of each layer of the crystal is h, which is the same as d for a monolayer and $0.816d$ for hexagonally close-packed multilayers.

First we consider the material balance in water flow. At steady state, the upward volumetric flow rate of water through the area defined by h_f and the substrate width (W)

is equal to the volumetric water evaporation rate from the meniscus above the area, and thus

$$j_w h_f = J_{evap}, \tag{2-7}$$

where j_w is the volumetric flux of water in the vertical direction through the area ($h_f \times W$). j_w consists of water flux from the surface layer ($j_{w,s}$), induced when microspheres are pushed by the barrier, and water flux from the bulk solution ($j_{w,b}$), induced by the upward substrate motion and Laplace pressure. Let α and $1 - \alpha$ be the weighting factor of the two fluxes respectively, so that the total water flux can be written as

$$j_w = \alpha j_{w,s} + (1-\alpha) j_{w,b}, \tag{2-8}$$

where we assume that α is a constant.

Next, we consider the balance in microsphere flow. We define the surface layer as the layer of thickness d where flow of water and microspheres is induced by the barriers' movement. The surface layer extends from the area where h_f is defined to the edge of the barrier. The volumetric flux of microspheres from this surface layer is denoted by $j_{p,s}$. Then the volumetric flow rate of microspheres in the surface layer is equal to that of microspheres formed in the top assembled layer:

$$j_{p,s} d = v_c h (1-\varepsilon), \tag{2-9}$$

where ε is the void fraction in the assembled layer. For the ideal case where the maximum order is achieved, the assembled structure would consist of a single crystalline domain of hexagonally close-packed (hcp) microspheres. In that case, ε is calculated to be 0.395 for monolayers and 0.260 for multilayers.

To bridge the gap between the two material balance considerations, we assume that the ratio of volumetric flux of water to that of microspheres in the surface layer is equal to the ratio of volume fraction of water to that of microspheres in the layer

$$\frac{j_{w,s}}{j_{p,s}} = \frac{1-\varphi}{\varphi}, \tag{2-10}$$

where φ is the volume fraction of the microspheres in the surface layer. This assumption is justified in our work because the assembly occurs at a fixed surface pressure. As we will see in the next section, a fixed surface pressure is equivalent to a fixed area per molecule, and thus the flow rate of a material from the surface layer must be proportional to the volume fraction of the material in the layer.

From Eq. (2-7)-(2-10), the expression for the substrate pulling speed can be written as

$$v_c = \frac{d}{(1-\varepsilon)hh_f}\frac{\varphi}{1-\varphi}\left[\frac{J_{evap}-(1-\alpha)j_{w,b}h_f}{\alpha}\right], \tag{2-11}$$

For the assembly of n^{th} layer, in Eq. (2-11), we approximate h_f and h as nd and d, respectively, so that

$$v_c \cong \frac{1}{(1-\varepsilon)d\alpha}\frac{\varphi}{1-\varphi}\left[\frac{J_{evap}}{n}-(1-\alpha)j_{w,b}d\right], \tag{2-12}$$

Equation (2-12) approximately expresses a condition for maximum order, where v_c increases linearly with increasing $\varphi/(1-\varphi)$. As shown later, v_c corresponding to the maximum order increases linearly with increasing $\varphi/(1-\varphi)$. The figure also shows that the y-intercept is nonzero. Therefore to complete Eq. (2-12), the equation must have a

term independent of $\varphi/(1-\varphi)$ that corresponds to the non-zero *y*-intercept. The only variable in Eq. (2-12) that can contain the independent term is $j_{w,b}$. Therefore, we separate $j_{w,b}$ into two terms: one that is dependent on and the other independent of $\varphi/(1-\varphi)$, when multiplied by $\varphi/(1-\varphi)$:

$$j_{w,b} = \frac{\alpha}{1-\alpha}\left[j_0 + \frac{1-\varphi}{\varphi}(1-\varepsilon) j_1 \right], \tag{2-13}$$

where j_0 and j_1 are constants. By substituting Eq. (2-13) into Eq. (2-12), the expression for v_c is

$$v_c \cong \frac{1}{(1-\varepsilon)d}\frac{\varphi}{1-\varphi}\left(\frac{J_{evap}}{\alpha n} - j_0 d \right) - j_1. \tag{2-14}$$

The microsphere volume fraction φ in the surface layer is simply the ratio between the volume occupied by the microspheres and the total volume:

$$\varphi = \frac{NV_p}{Ad}, \tag{2-15}$$

where A is the area between the substrate and the barrier, N is the number of microspheres confined in the area, and V_p is the volume of a single microsphere. Substituting Eq. (2-15) into Eq. (2-14), we have

$$v_c \cong \frac{1}{(1-\varepsilon)d}\frac{1}{\frac{Ad}{NV_p}-1}\left(\frac{J_{evap}}{\alpha n} - j_0 d \right) - j_1. \tag{2-16}$$

Equation (2-16) indicates that as the area per microsphere *A/N* in the surface monolayer on the water subphase decreases, the substrate pulling speed must increase to maintain the constant porosity in the assembled vertical monolayer. In practical terms,

this implies that if more microspheres are introduced to the surface layer, the pulling speed must increase to achieve maximum order. We also observe that the surface pressure increases as A/N decreases (as shown in the next section). Therefore, as the surface pressure increases (i.e., as A/N decreases), the pulling speed must also increase to maintain the maximum order. This implication from our model is rather unexpected since, in previous studies in optimization of LB assembly, the optimal surface pressure has been determined irrespective of the pulling speed. [61,63,64] On the contrary, our modeling suggests that the two independent parameters must satisfy the relation in Eq. (2-16) to achieve maximum order.

2.5 Langmuir-Blodgett isotherms

As mentioned previously, LB isotherm is an equation of state that describes a relationship between area, occupied by particles, per particles and surface pressure. The isotherm gives insight into interactions between particles and between particles and a subphase. In practical terms, the isotherm provides guidance on finding appropriate conditions for LB assembly. Generally, it is advisable to measure an LB isotherm before fabricating samples with LB assembly, and it is useful to monitor the isotherm during LB assembly as well.

The LB isotherm experimentally measured for our system is shown in Fig. 2.4 as black circles. For area per molecules (A/N) below ~1.23 μm^2 the surface pressure remains approximately unchanged. This is due to distance between microspheres being significantly greater than their associated Debye length, resulting in microspheres not interacting with one another. The surface pressure increases sharply as the effective

projected area per microsphere approaches ~1.20 μm^2, which represents the monolayer collapsing point. Based on this area, the center-to-center average distance between two microspheres at the collapsing point is calculated to be ~1.2 μm. When the microspheres of 0.9 μm in diameter form a hexagonally close-packed monolayer, the center-to-center distance would be 0.9 μm, and the effective projected area per microsphere would be 0.701 μm^2. Therefore, a monolayer in our LB system collapses when the average distance between the microspheres is close to but greater than their diameter. This observation is in agreement with previous studies. [43,65]

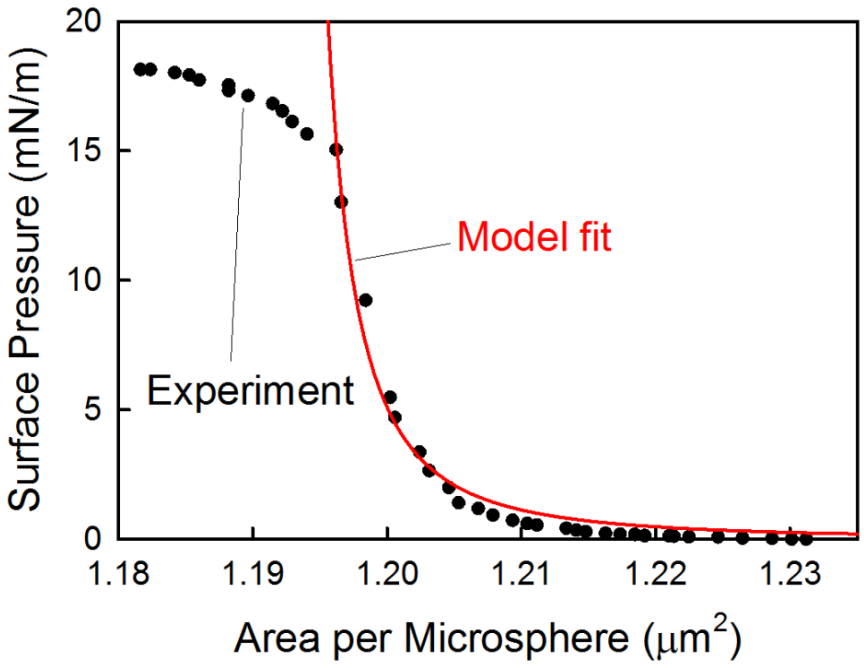

Figure 2.4. Experimentally determined LB isotherm (black circles) and a fitting to the 2D van der Waals equation of state (red curve).[†]

With this isotherm, we speculate that the sphere-to-sphere interaction is repulsive and thus, at the inter-distance close to 1.2 μm, it is more energetically favorable for the layer to collapse and form islands of multilayer instead of reducing the distance further.

Formations of such islands are confirmed in our experiments where the film is allowed to reach above the collapsing point (Figure 2.5). The slower rate of increase in the surface pressure above the collapsing point can also be explained in a similar fashion as well. Because formation of islands is more energetically favorable, the increase in surface pressure associated with this mechanism must be lower than that associated with reduction in the inter-distance below the collapsing value. We note that the difference between the distance at the collapsing point and the microsphere diameter can be smaller [66,69] than the current value of ~0.3 μm. Such difference depends on many system parameters, such as barrier speed, microsphere charging, degree of functionalization, polydispersity, temperature, etc.

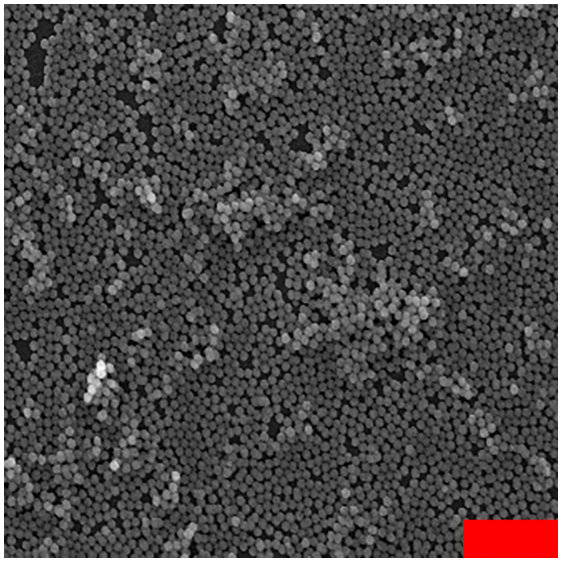

Figure 2.5. Scanning electron micrograph of an LB film deposited at a surface pressure above the collapsing point. The red scale bar represents 10 μm.

The isotherm also provides us guidelines for LB assembly in our work. First, for control of randomness, the monolayer should not be allowed to collapse and therefore the surface pressure should be below ~15 mN/m. In our work, it is observed that the pressure

rise becomes sharper as a function of time as the pressure approaches 15 mN/m. Therefore, it is recommended to use surface pressure lower than that value for the assembly. Second, surface pressure lower than 2 mN/m should not be used for LB assembly. Such low pressure corresponds to the lack of inter-particle interaction and thus significant voids between microspheres, which is not desirable for this work.

We fit the isotherm to the following 2-dimensional van der Waals equation of state:

$$\pi = \frac{k_B T}{\left(\frac{A - A_0}{N} - b\right)} - \frac{a}{\left(\frac{A - A_0}{N}\right)^2}, \tag{2-17}$$

where a is the microsphere interaction parameter, $b = \pi d^2/2$ is the excluded area of a particle, T is the solution absolute temperature, k_B is the Boltzmann constant, and A_0/N is the difference between the effective projected area per microsphere for the monolayer collapsing point and that for the ideal close-packing. Since this equation is used for describing 2-D interaction, it cannot describe the interaction beyond the collapsing point (where multilayer islands are form and the interaction becomes 3-D). Thus, we set a and A_0/N as fitting parameters and fit only the data for $A/N \geq 1.195$ μm^2. The model fit is shown as a red line in Figure 1.4 and is in good agreement with our experiment (a coefficient of determination of 0.984). The values, $a = -4.053 \times 10^{-13}$ $N \cdot \mu m^3$ and $A_0/N =$ 1.191 μm^2, are obtained from the fitting. The negative value of a indicates that the interaction between the microspheres is repulsive, suggesting that the electrostatic repulsion is stronger than van der Waals attraction. Thus, our speculation of the repulsive nature of the interaction is supported by the isotherm. However, 2-dimensional van der

Waals equation of state is only a simplified model for describing the interaction of microspheres in the LB trough and can only provide a semi-quantitative description. Therefore, while it is reasonable to conclude that the interaction is repulsive, we should not use the fitted value of a for a purpose of accurately quantifying the interaction. In practice in this work, the isotherm is mainly used for relating the area to the surface pressure as it is often more convenient to control surface pressure during an LB assembly.

2.6 Experimental results and comparison to the model

To test our model, we measured the average crystalline domain size, G, at various pulling speeds and surface pressures. Figure 2.6(a) shows the experimentally measured G values of a monolayer as a function of surface pressure (π) at different pulling speeds (v_c). For the surface pressures of 4.6, 6.0, and 8.0 mN/m, the pulling speeds that correspond to the maximum G values are 1.5, 1.8, and 2.25 mm/min, respectively (point c, d, e). This trend implies that pulling speed must increase as the surface pressure increases to maintain the maximum order. We can relate the optimal pulling speeds to the volume fractions, φ, by using Eq. (2-15) and Eq. (2-17). Using the relations, we plot the v_c at the maximum order for the three surface pressures as a function of φ / (1- φ) (black circles) and fit it to a linear model (dash red line) in Figure 2.6(b). The figure shows that v_c increases approximately linearly as φ / (1- φ) increases. This result is consistent with the prediction from our model in Eq. (2-14).

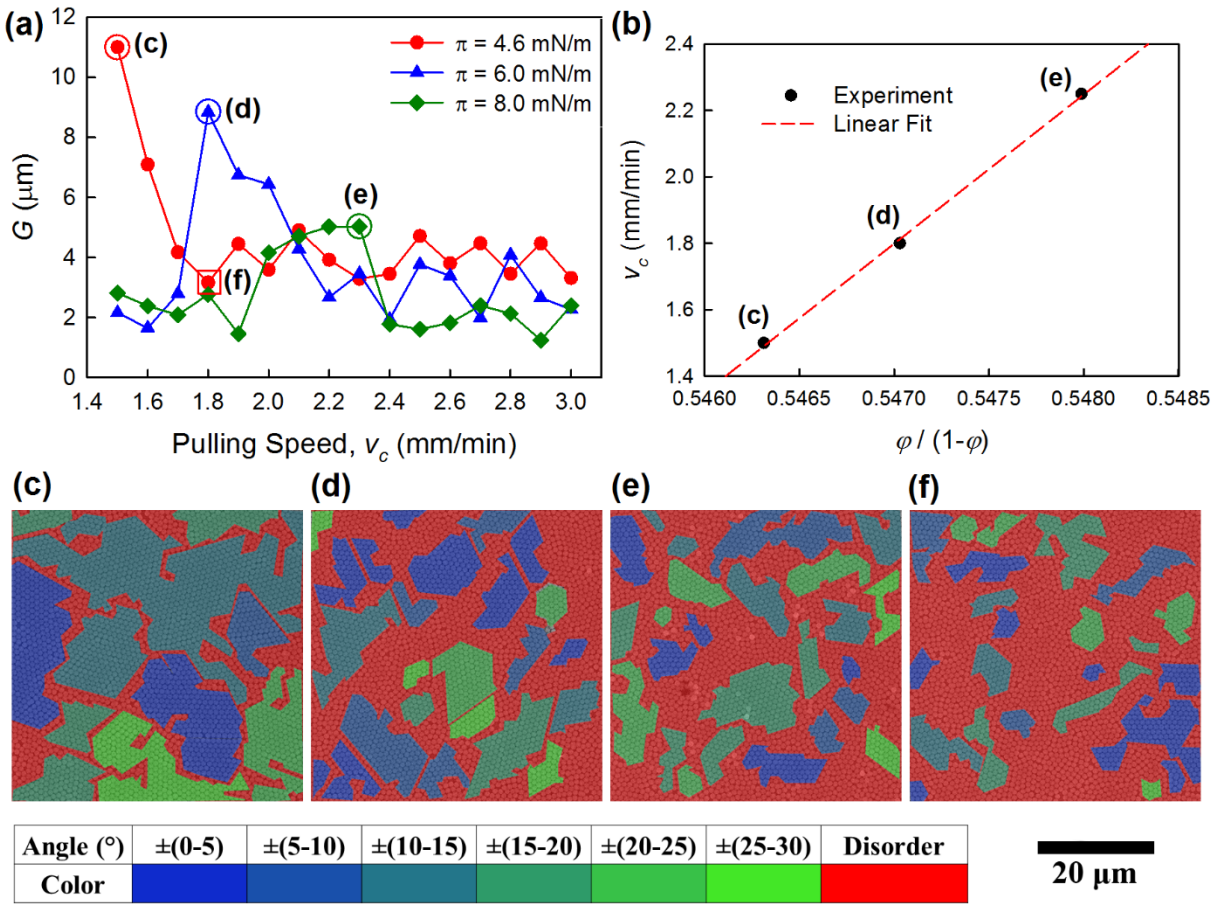

Figure 2.6. (a) Crystalline domain sizes determined at various values of surface pressure and pulling speed for a monolayer assembly. (b) v_c as a function of j /(1−j) for the (c)-(e) points in (a). (c)-(f) Representative SEM images corresponding to the monolayer assembly conditions indicated as (c)-(f) in (a). For the convenience of view, the crystalline domains are colored depending on the orientation from blue to green and the disordered regions are painted red. †

A key observation in Figure 2.6(a) is that the G values can be highly sensitive to the pulling speed at a given surface pressure, abruptly changing over a narrow range of v_c. For instance, at π = 6.0 mN/m, G dramatically decreases from >8.8 μm to 2.8 μm when the pulling speed decreases from v_c = 1.8 mm/min to 1.7 mm/min (point (d) in Fig.

2.6(a)). This high sensitivity suggests that the introduction of disorder in the LB assembly should be performed carefully at precise values of surface pressure and pulling speed. Specifically, when the degree of randomness is to be increased slightly, change in pulling speed should be made along with the linear trajectory described by the model. Arbitrary adjustment in the pulling speed may lead to a significant change in G and a significant disruption in order. We note that, while significant disorder may be desirable in many applications, there are more efficient methods to fabricate such samples, which will be discussed in a later chapter.

To visualize the dependence of G on the experimental conditions, we took scanning electron micrograph (SEM) 50μm×50μm images of the samples corresponding to (c)-(f) points in Fig. 2.6(a), as shown in Fig. 2.6(c) – (f). The disordered regions are highlighted in red and the crystalline domains in blue and green. Small point defects in crystalline domains are ignored in the coloring. The shades of color between blue and green represent different orientations of the crystalline domains. The orientation is characterized by the angle between a lattice vector and the horizontal line in the figures. Due to the 6-fold rotational symmetry of the lattice, the angle is between ±30°. The total area of red regions (disorder) in Fig. 2.6(f) is much greater than that in Fig. 2.6(c). This increase in disorder is consistent with the decrease in G for π = 4.6 mN/m in Fig. 2.6(a) as we expect. Another observation is that, in Fig. 2.6(c), the disordered regions form irregular thin lines between large single crystalline domains. On the contrary, in Fig. 2.6(f), the disordered regions take a large space between the small crystalline domains. Note that the G values are obtained from a large area of ~5 mm^2 by laser diffraction, while the SEM images are taken over a smaller area of 2.5×10^{-3} mm^2. Therefore, the G

value is a much better representation of the structural order/disorder than the SEM images. In our work, the trend in *G* value agrees well with the trend observed in the SEM images.

From these observations from Fig. 2.6, we can surmise a mechanism of formation of structural order in the LB assembly. Initially, microspheres are randomly positioned. As the area between barriers decreases, some microspheres start to form small crystalline domains on the subphase surface. [70] The small crystalline domains are randomly oriented on the liquid surface. As the microspheres are transferred onto a substrate at the optimum pulling speed and surface pressure, these small crystalline domains appear to grow to form larger domains, while microspheres that are not in the crystalline domains become disordered regions. When the assembly is not performed under the optimum condition, the microspheres are not closely packed, and the crystalline domains do not significantly grow. Consequently, the disordered areas are large and thus the LB film is more disordered.

We also speculate that the growth of crystallographic domains has an associated characteristic time scale. Since enough time must be provided for the domains to grow, the structural order is likely to improve with decreasing pulling speed, provided that the pulling speed and the surface pressure are both maintained at the optimum condition described by Eq. (2-16). This speculation is supported by the results shown in Fig. 2.6(a), where the maximum *G* value increases from 5.0 to 8.8 to 11.0 μm as v_c decreases from 2.25 to 1.8 to 1.5 mm/min. The visual comparison between Fig. 2.6(c)-(f) further supports our speculation that the crystalline domain orientation is random, and the domain size increases as the pulling speed decreases while meeting the optimum

conditions by Eq. (2-16). However, when the optimum condition is not satisfied at the same pulling speed (1.8 mm/min), going from Fig. 2.6(d) to (f), the average domain size becomes smaller, while the orientation distribution still appears similarly random. This understanding of structural ordering mechanism provides a simple method to introduce a small degree of randomness into the structure: we increase the pulling speed while adjusting the surface pressure to be at the optimum condition. In this way, the crystalline domains can grow and their sizes are controlled by the pulling speed.

The level of structural order in multiple layers, where the number of layers (n) varies from 2 to 8, is also investigated. To determine how the optimum surface pressure depends on the number of layers in the LB assembly, we fix the pulling speed at 1.5 mm/min and determine the optimum surface pressure that maximizes G for each layer in the multilayer structure. Figure 2.7(a) shows this optimum surface pressure as a function of n (red circles). The results show that the optimum surface pressure must increase as the number of layers increases. For the first three layers, the optimum surface pressure increases rather steeply as the number of layers increases. For the number of layers greater than 3, the optimum surface pressure increases more gradually for the maximum order.

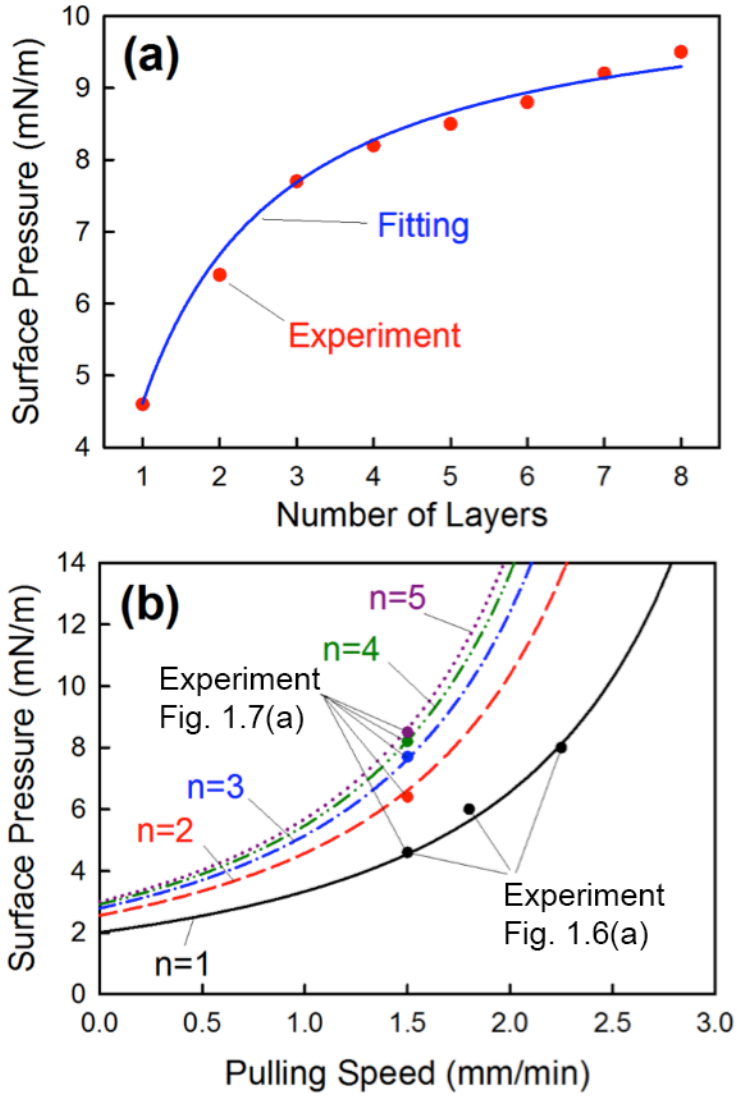

Figure 2.7. Dependence of optimum surface pressure on (a) the number of layers and (b) the pulling speed for various numbers of layers for maximum order in LB microsphere assembly.[†]

This dependence of the optimum surface pressure on n again agrees with our model in Eq. (2-16). From Eq. (2-16), we can express A/N in terms of n as

$$\frac{A}{N} = \frac{V_p}{d}\left[\frac{J_{evap}}{(1-\varepsilon)\alpha d(v_c + j_1)} \cdot \frac{1}{n} + 1 - \frac{j_0}{(1-\varepsilon)(v_c + j_1)}\right]. \qquad (2\text{-}18)$$

j_1 is determined to be positive from the linear fit in Fig. 2.6(b), and therefore *A/N* decreases as *n* increases according to Eq. (2-18). Also, according to the LB isotherm, *A/N* decreases as the surface pressure increases. Therefore, the surface pressure increases as *n* increases, as observed in our experiment in Fig. 2.7(a). In fact, the least square fit to Eq. (2-18) with two fitting parameters agrees well with the experimental data shown in Fig. 2.7(a) (a coefficient of determination of 0.995). The two non-dimensional fitting parameters are $\frac{J_{evap}}{(1-\varepsilon)\alpha d(v_c + j_1)}$ and $1-\frac{j_0}{(1-\varepsilon)(v_c + j_1)}$. All these results so far have shown that our model has successfully described the relationship between various assembly parameters for optimal conditions.

To further show the implication of Eq. (2-16) that governs maximum order in LB assembly, we consider Fig. 2.7(b), which shows surface pressure as a function of pulling speed for the n^{th} layer, using the two fitting parameters. Each line represents a trajectory for optimum condition for maximum possible order. The experimentally determined optimum points found in Fig. 2.6(a) and 2.7(a) are also displayed in Fig. 2.7(b) (circles). The model curve shows good agreement with the experimental data. According to the model calculations, the surface pressure must increase as the pulling speed or the number of layers increases. For large v_c and π, the optimum surface pressure increases sharply as the pulling speed increases. In prior studies, the pulling speed ranged from 1 to 10 mm/min. [63,65,69,71] If one is to use a high pulling speed, extra care is required when controlling the optimum surface pressure because of the strong dependence between the two parameters. Another consideration is that the surface pressure cannot be increased

above the point where the monolayer collapses. Therefore to have the most flexibility in introducing the disorder, it is recommended to begin the LB process with low surface pressure and thus low pulling speed.

In summary of the results, the guideline for controlled introduction of randomness in LB assembly is the following. The process should start from the optimum pulling speed and pressure, preferably at low values, for the given n^{th} layer and then gradually increase the pulling speed while adjusting the surface pressure to satisfy Eq. (2-16). The surface pressure should also be lower than the collapse pressure.

2.7 Conclusion

In this Langmuir-Blodgett work, we have demonstrated how structural randomness can be controllably introduced into periodic structures during the LB assembly of microspheres. Specifically, we have investigated the relation between two process parameters: surface pressure and substrate pulling speed. We have showed that, to maximize the structural order and thus for minimal randomness, the two parameters must satisfy a relation derived from material balance considerations and Langmuir-Blodgett isotherm. We observed that a small deviation from this relation can introduce a large degree of randomness and this destroy structural order. To controllably introduce randomness, we find that one should start the assembly from optimum pulling speed and surface pressure that satisfy their interrelation (Eq. (2-16)) for a given n^{th} layer, but gradually increase the pulling speed. During this increase, one will have to adjust the surface pressure to satisfy Eq. (2-16).

Overall, we expect that our findings will prove useful in mimicking biological photonic structures, as they incorporated significant degree of randomness in periodic patterns. In our future work, we aim to investigate how the randomness in ordered structures influences optical properties such as angle-dependent reflectance and emissivity. Further studies on the control of disorder in LB assembly can also be pursued by considering energetics of 2D colloidal crystallization, in addition to material balance done in this work. Such studies would provide insight into fundamental physics that governs the LB assembly.

Portions of this chapter have been published as S. Atiganyanun, M. Zhou, O. K. Abudayyeh, S. M. Han, and S. E. Han, Langmuir **33**, 13783 (2017) and are reproduced with permission of the publisher.

[†]Figure reproduced with permission from S. Atiganyanun, M. Zhou, O. K. Abudayyeh, S. M. Han, and S. E. Han, Langmuir **33**, 13783 (2017).

Chapter 3: Disordered Microsphere-based Coatings for Efficient Radiative Cooling

*Reproduced in part with permission from S. Atiganyanun, J. B. Plumley, S. J. Han, K. Hsu, J. Cytrynaum, T. L. Peng, S. M. Han, and S. E. Han, ACS Photonics **5**, 1181 (2018). DOI: 10.1021/acsphotonics.7b01492.

3.1 Overview

Radiative cooling is a process where a net heat loss through thermal radiation is achieved. The thermal radiation from a terrestrial object in a select mid-infrared (IR) spectral range, known as the atmospheric transparency window, can transmit through the atmosphere into the space. When this heat loss is greater than the heat gain from ambient sources, the object cools below ambient temperature until it reaches a thermal equilibrium where the net heat transfer is zero. [54,57,72] While radiative cooling technology has become a prominent topic in research recently, its capability has been demonstrated 50 years ago. In 1963, Trombe demonstrated that this cooling effect can reduce the object temperature by ~35 °C below the ambient temperature at night. [54] Recently, a seminal work by Raman et al. in 2014 [57] showed that radiative cooling of an object by 5 °C below the ambient temperature under direct sunlight can be achieved. Indeed, commercial paint products that employ radiative cooling technology are already available in the market and achieved a similar degree of cooling during the day time. [73]

For daytime cooling, the other desired property is to strongly scatter or reflect that sunlight to minimize solar heating. To achieve this, sophisticated nanostructures were used in the past. [57,58] Alternatively, a thin silver film can maintain the solar

absorptivity below 4% without the nanostructures. [58] While other metal films can also reflect the sunlight, most metals absorb more strongly than silver. A 1% increase in the solar absorption over silver corresponds to an increase of the heat absorption by ~10 W/m^2. Because, at the ambient temperature, the cooling power is around 100 W/m^2 [59], the 1% increase in solar absorption would lead to a decrease in the cooling power by 10%. With this understanding, recent studies have combined a silver film with dielectric materials of high solar reflectance for efficient radiative cooling under sunlight. [57–60] In some of these studies, the cooling materials are in a form of a thin flexible sheet, where silver is the material primarily responsible for solar reflection. [59,60] Although the previous studies using silver have achieved great cooling performance, it would be desirable for practical applications to avoid the use of such expensive metal films and their deposition processes. It would also be preferable to have the cooling materials in a simpler format such as paint. [73–77] Indeed, some commercial solar reflective paints [73] achieve a cooling performance comparable to the recent works in academia. With these innovations in consideration, we aim to conduct a study of optical scattering in random media comprised of materials with intrinsically high mid-IR emission.

Common pigments found in commercial solar-rejection white paint include TiO_2 particles of 200-250 nm in size [78,79] and hollow spheres of relatively low refractive index (~1.5) with the size of 50-150 μm. [73] While these particles have strong mid-IR emission, they suffer from strong UV absorption or weak solar scattering. Specifically, TiO_2, a high refractive index material, has significant absorption of UV light, which accounts for 5% of total solar intensity. [79] For hollow spheres, low refractive index materials lead to inefficient light scattering. Because the intrinsic UV absorption in high-

index particles is difficult to eliminate, we choose to use a low-index SiO_2 microspheres to create solar scattering disordered media. Because silica also has an intrinsic high emissivity in the atmospheric transparency window, the goal of this work is to optimize the scattering in the solar region of the microsphere-based disordered structures. We will show that, with right particle size and disorder, these randomly packed microspheres, fabricated with inexpensive and facile techniques, can surpass the cooling performance of the commercial paint products.

3.2 Fabrication of disordered microsphere-based structures

Two fabrication methods used in this work are colloidal sedimentation and spray coating. Both are described below.

The first method follows the work of Garcia et al. [46] who first introduced photonic structures that consisted of polymer monodisperse microspheres arranged in a completely disordered fashion. The fabrication method exploits the nature of the stability in a colloidal solution. While the subject of colloidal stability has a long history [46,80] and involves a large degree of complexity due to many-body Coulomb interactions, a recent work by Wu and Lai [81] has elucidated this nature of the interaction and succeeded in accurately describing the early stage coagulation of a colloidal suspension. In a short summary, the interaction between two colloidal spherical particles can be expressed as a sum of two potentials: the electrostatic repulsive potential and the attractive Van der Waals potential. The electrostatic repulsive potential acts as a barrier that prevents flocculation of colloids and maintains the stability. This repulsive potential, however, can be attenuated by a presence of electrolytes. This attenuation can be so

significant that the electrostatic potential becomes weaker than the Van der Waals potential, resulting in a net attractive interaction and thus flocculation. Disordered clusters formed during the flocculation sediment onto a substrate and leave a disordered coating once a solvent evaporates.

In this work, we adopt the fabrication method for silica microspheres. Essentially, silica microspheres are first dispersed in water and then filtered to improve monodispersity. An ionic aqueous salt solution is then introduced into the solution and causes the flocculation. The solution is transferred to a substrate and its solvent evaporates, leaving a disordered coating behind. The thickness of the coating is controlled by the total volume of the colloidal solution.

The spray coating method is a widely used technique for applying many coatings for a great variety of applications. In the spray coating process, a liquid is accelerated by high velocity fluid such as pressurized gas, which atomizes the liquid into small droplets. The droplets are deposited onto a substrate, creating a film. The complete picture of mechanism of the atomization process is complicated and dependent on various parameters such as air pressure, liquid flow rate, liquid viscosity, liquid surface tension, substrate temperature, and droplet travel distance. [82–87] Due to a stochastic nature of the atomization, droplets of a microsphere solution can be used to transfer the microspheres in a disordered manner onto a substrate, creating a coating of randomly arranged microspheres. One important consideration is that microspheres can rearrange when they are already deposited onto a substrate if there is still some solvent in the film. This rearrangement can induce order and therefore must be prevented.

One important aspect for these two methods, especially the spray coating, is that they are very facile and scalable. They also do not involve costly instruments that are used in previous works. Since our films will consist of only silica microspheres, the material cost is significantly lower than other films that use expensive silver. If structures fabricated by these methods can achieve efficient radiative cooling, these techniques can serve as a way to bring the radiative cooling technology into wide scale applications.

3.3 Transport mean free path of the disordered system

Light scattering in random media strongly depends on their structures and randomness. Because of the complexity of the light interaction in a random medium, diffusion approximation is invoked to model the light propagation. [88] In this model, the key parameter is a transport mean free path (l^*), which is an average distance that light has to travel before its propagation is no longer correlated with its original propagation direction. The transport mean free path is related to the degree of the randomness: l^* increases as the randomness decreases. More importantly, light scattering from a random medium increases as l^* decreases. Thus, toward the goal of maximizing the solar scattering efficiency, we seek to minimize the transport mean free path of our disordered structures in the solar spectrum.

In an isotropic random medium, the transport mean free path is related to total optical transmittance (T) and the medium's thickness (L) by [89,90]

$$T = \frac{l^*(1+z_e)}{L+2z_e l^*}, \tag{3-1}$$

where z_e is an extrapolation length ratio, whose dependence on internal reflectance, R, is given by

$$z_e = \frac{2(1+R)}{3(1-R)}. \tag{3-2}$$

One can approximate the internal reflectance by using Maxwell-Garnett effective medium approximation to calculate the effective refractive index of the disordered layer. [91] We also note that T is a function of wavelength and, by applying linear regression to Eq. (3-1) to estimate the slope $1/(l^*(1+z_e))$, l^* as a function of wavelength can be extracted.

We also seek to theoretically investigate how l^* is related to fill fraction and microsphere size. We use mean field theory and coherent potential approximation [92,93] to calculate the dependence. The system is modeled by two scattering units surrounded by an effective medium. [93] One unit is en empty microsphere, and the other unit is a solid SiO_2 microsphere concentrically surrounded by an empty sphere. Light propagation in the effective medium is characterized by a complex wave vector $k + i/(2l)$, where l is the scattering mean free path, an averaged distance between scattering sites. The l is calculated by requiring that the forward scattering amplitude is zero on average when the scattering units are within the effective medium. Using a relation between l and l^* in the low concentration limit [92] (applicable to our structures),

$$l^* = \frac{l}{1-\langle \cos\theta \rangle}, \tag{3-3}$$

where $\langle \cos\theta \rangle$ is a value of cosine averaged over all scattering amplitudes, we calculate l^* from the knowledge of l.

For a large-sphere system, we can apply Kubelka-Munk theory [94] to facilitate the l^* calculation. For lossless sphere, the transmittance is given by

$$T = \frac{1}{SL+1}, \tag{3-4}$$

where S is the scattering coefficient and is related to the effective scattering efficiency, Q_{eff}, by [95]

$$S = \frac{3f}{2d} Q_{eff}. \tag{3-5}$$

The value of Q_{eff} is different from the scattering efficiency of a single sphere, Q, because of interactions between spheres. An empirical correlation between the two are given by [96]

$$Q_{eff} = Q10^{-10^{0.25-5.1c/\lambda}}, \tag{3-6}$$

where c is estimated to be [97]

$$c = d(\frac{0.905}{f^{1/3}} - 1). \tag{3-7}$$

For large spheres, the size parameter $\pi d/\lambda$ is much greater than 1, and thus Q can be set equal to 1. Further, for random packing, $f \leq 0.64$ and $Q_{eff} \sim Q$ for the large size parameter. Therefore, for large spheres, Eq. (3-4) becomes

$$T = \frac{1}{\frac{3f}{2d} L + 1}. \tag{3-8}$$

Comparing this equation to Eq. (3-1), we see that $z_e = 1$ and $l^* = d/3f$.

3.4 Experimental methods

i) Colloidal sedimentation method

0.9-μm-diameter and 2.0-μm-diameter solid silica microspheres were purchased from Fiber Optic Center (AngstromSphere) in a powder form. Before the microspheres of either size can be used, agglomerations must be broken down and filtered. First, the microsphere (of a same size) powder was dispersed in deionized water, and the solution was sonicated for an hour. Then the solution was filtered with a VWR Grade415 filter paper to remove any agglomerations left. The solution was diluted to 2% volume, and 0.01M of KCl was added. The salt addition induced colloidal instability, and the microspheres flocculated and precipitated onto a glass slide as a randomly packed film. On a glass slide, we used a Scotch Magic tap to create a barrier that confined the solution and specified an area that the coating will be created. For the purpose of measuring transport mean free path, several coatings were fabricated with varying thickness and each coating was confined to a 2.5cm-by-2.5cm area.

ii) Spray coating method

The same microspheres were used for the spray coating method. 2% volume aqueous solution of 0.9-μm-diameter microspheres (without KCl) was prepared. Optionally, a surfactant at a concentration lower or equal to 2×10^{-3} % can be introduced to the solution. The solution was then ejected through an air-brush nozzle (Badger 100G, Badger Air-Brush), shown in Fig. 3.1, at 69 kPa. In this process, the microsphere solution was added to the cup and the compressed air was introduced via the attached hose. The

flow of both fluids was regulated by the trigger and the needle. When the trigger was pulled, both fluids were mixed and the solution was atomized into droplets ejected through the head of the gun. For consistency of the flow, we pulled the trigger fully in during deposition. The spray coating condition was identical for a solution of 2 μm microspheres. The nozzle was located 22.5 cm above a glass substrate. To ensure uniformity, the substrate was subjected to a linear periodic motion and was heated at above 100 °C to quickly remove water. The rapid water removal is essential for preventing significant arrangement of microspheres, which can occur if the water evaporation is slow. It is noted that mechanical strength of the coating grows weaker as the thickness increases. Thus the spray coating should not continue once deposited microspheres on a sample begin to be ejected by the airflow.

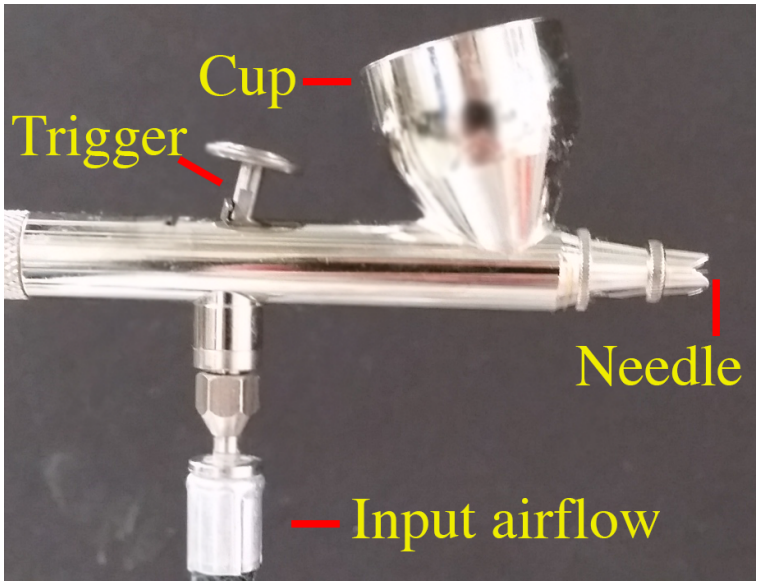

Figure 3.1. An image of a spray paint gun used in this work. Distance from the needle to the left edge of the image is ~8.5 cm.

iii) Optical and structural characterization

For transport mean free path measurement, randomly packed SiO_2 microsphere films of thickness varying from 20 to 100 μm were fabricated via both colloidal sedimentation method and spray coating method. Total transmittance of the coatings was measured with an integrating sphere (ISO-50-8R, Ocean Optics) and a photospectrometer (USB4000-VIS-NIR, Ocean Optics). A scanning electron microscope (FEI Q3D FIB/SEM DualBeam system, ThermoFisher Scientific) was used to observe arrangement of microspheres on a coating surface and to measure the coating thickness. Using the refractive index of silica (n = 1.46) and the fill fraction range (f ~ 0.55 to 0.64), we applied Maxwell-Garnett effective medium approximation and calculated the extrapolation length ratio to be 1.4. [91] Knowing the ratio, we fitted for transport mean free path spectrum from the total transmittance spectrum and the thickness, using Eq. (3-1). Emissivity spectrum, from UV to IR, of the disordered coatings was measured by a spectrophotometer with an integrating sphere (Vertex 70, Bruker).

iv) Temperature measurement

For evaluating the radiative cooling performance of our coatings under the sunlight, we deposited 2-μm microspheres on 2.5 cm × 2.5 cm glass substrates, using the colloidal sedimentation method. To fabricate coatings appropriately thick for solar rejecting, the colloidal sedimentation method was repeated several times on a same substrate. The coating thickness was ~700 μm. The bottom of the glass substrate was also painted black (Specialty Black High Heat Ultra, Rust-Oleum). For comparison, we prepared a sample where our microsphere coating was replaced by a commercial solar reflective white paint (Spartacryl PM 60312, Chromaflo Technologies) with the same thickness (and the same black paint on the bottom side). This commercial paint was

selected because we experimentally determined that it had the lowest temperature under the sunlight among several different brands of solar reflective paints.

To characterize the cooling properties of the samples under the sunlight, we set up fixtures shown in Fig. 3.2. This experimental setup is designed to accurately measure the temperature of the air around the samples. Thus the setup allows the sample temperature to be properly compared to the ambient air temperature. Typically in other works, the ambient temperature is measured in a Stevenson screen, which comprises of a white-painted box with slits on its side walls to allow air flow. The white surfaces minimize the solar radiative heating of the box. The inside of the box is also dark enough to prevent radiative heating of a thermometer in the box. The thermometer is generally located about 1-2 m above the ground. Our fixtures are modified from a Stevenson screen to allow the temperature measurement of samples exposed to the sunlight. Our box had a 30 cm × 30 cm window at the top which allows the sunlight to reach the sample. The bottom of the box is sealed by a low-density polyethylene (LDPE) film that is optically transparent to prevent the solar heating from the light coming through the top window. Additionally, the sides walls do not have slits and thus reduced the fluctuation in the inside temperature caused by air convection. The walls are made of Styrofoam covered with aluminum sheets on their exterior to minimize the sunlight transmitted through the walls.

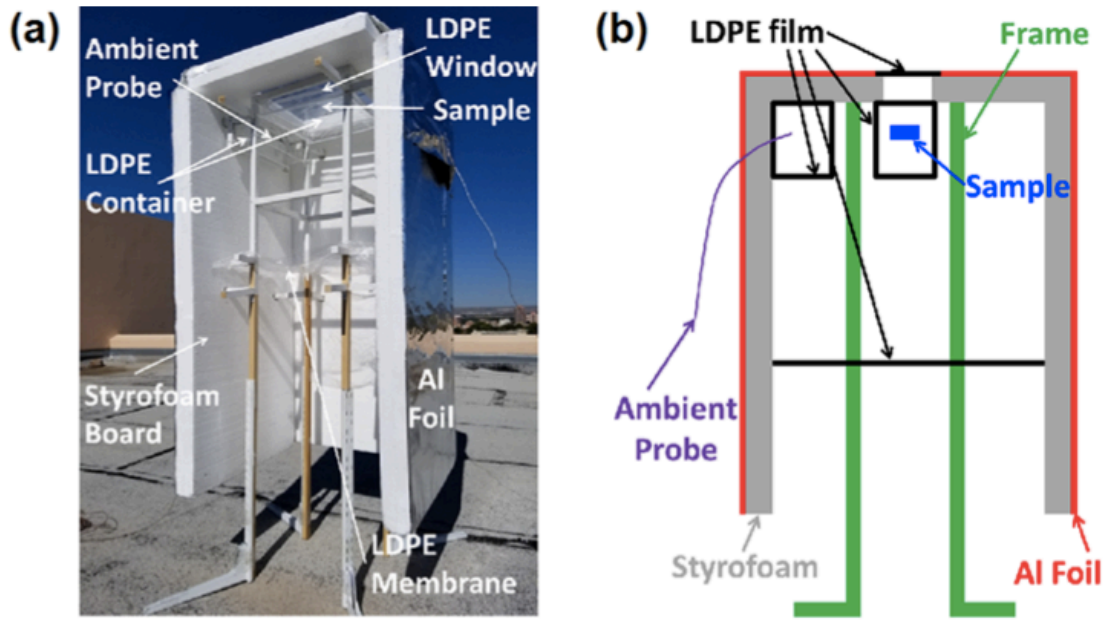

Figure. 3.2. (a) Optical image and (b) schematic diagram of the outdoor setup for accurate temperature measurement. The height of this apparatus is ~1.5 m. †

Two LDPE enclosures of a 2360 cm^3 volume are located inside the setup, one beneath the top window and the other beneath the top cover. Thermocouples for the sample and the ambient air are placed inside the two enclosures, respectively. Having the two separate volumes minimizes the heat transfer between the thermocouples. The enclosure for the ambient temperature measurement is located far from sunlight illumination even at the low sun's altitude. Both thermocouples are located 2 m above the ground. This is to avoid any heat transfer from the heated ground to the thermocouples. In our design, the ambient temperature represents the temperature of the air surrounding the sample while minimally affected by the sample temperature and the ground temperature. This enables proper and fair characterization of the cooling performance in comparison to the ambient temperature.

With this setup, the temperature of the samples and the ambient air under strong solar radiation in Albuquerque, New Mexico was measured in May when the sky was relatively clear. During the time, two setups, one for our coating and one for the commercial paint, were placed on a rooftop of a building. The temperature of the two samples and the ambient air was recorded for 3.5 days.

3.5 Results and discussion

For illustration purpose, an optical image of the silica microsphere-based coating under light illumination is shown below in Fig. 3.3.

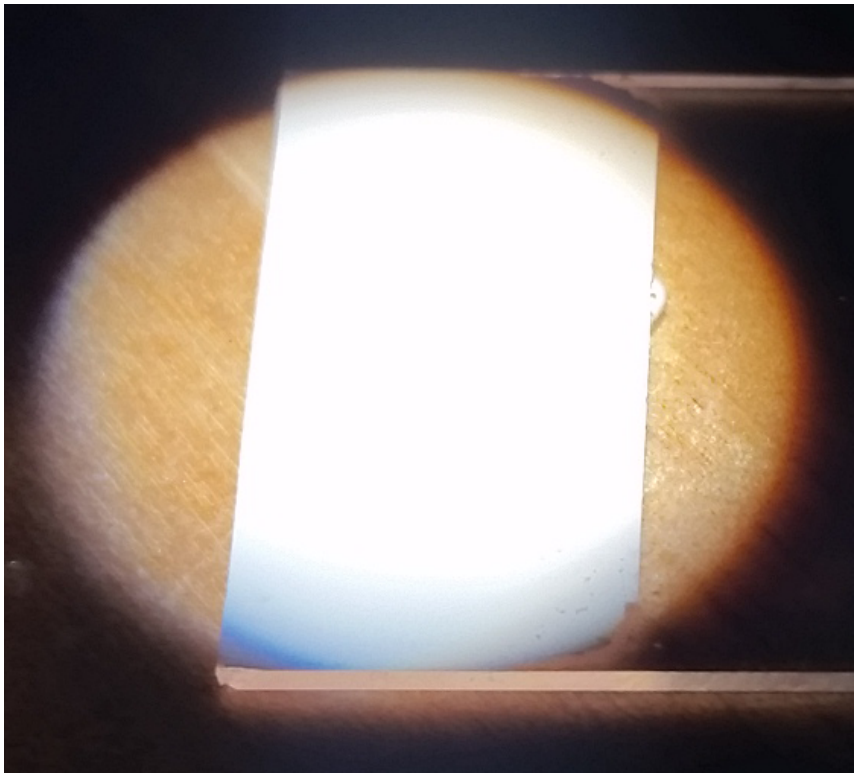

Figure 3.3. Our disordered silica microsphere-based sample under light illumination.

i) Measured and modeled transport mean free path

Both experimentally measured and theoretically calculated l^* as a function of wavelength for the samples with 0.9-μm-diamter microspheres is shown in Fig. 3.4. The samples prepared by colloidal sedimentation and spray coating exhibit a similar l^* spectrum. For these samples, the calculated result for the fill fraction of 0.64, which corresponds to random close packing [98], demonstrates an excellent agreement with the experimental result. Additionally our model also accurately captures the resonant behavior in l^* that appears as valleys and peaks in Fig. 3.4. In comparison, the results from other theoretical models in previous studies [99,100] show a significant divergence from the experimentally measured l^*. In these studies [99,100], the models predict a trend where l^* decreases as the wavelength increases, which is opposite to the trend shown in the experimental results.

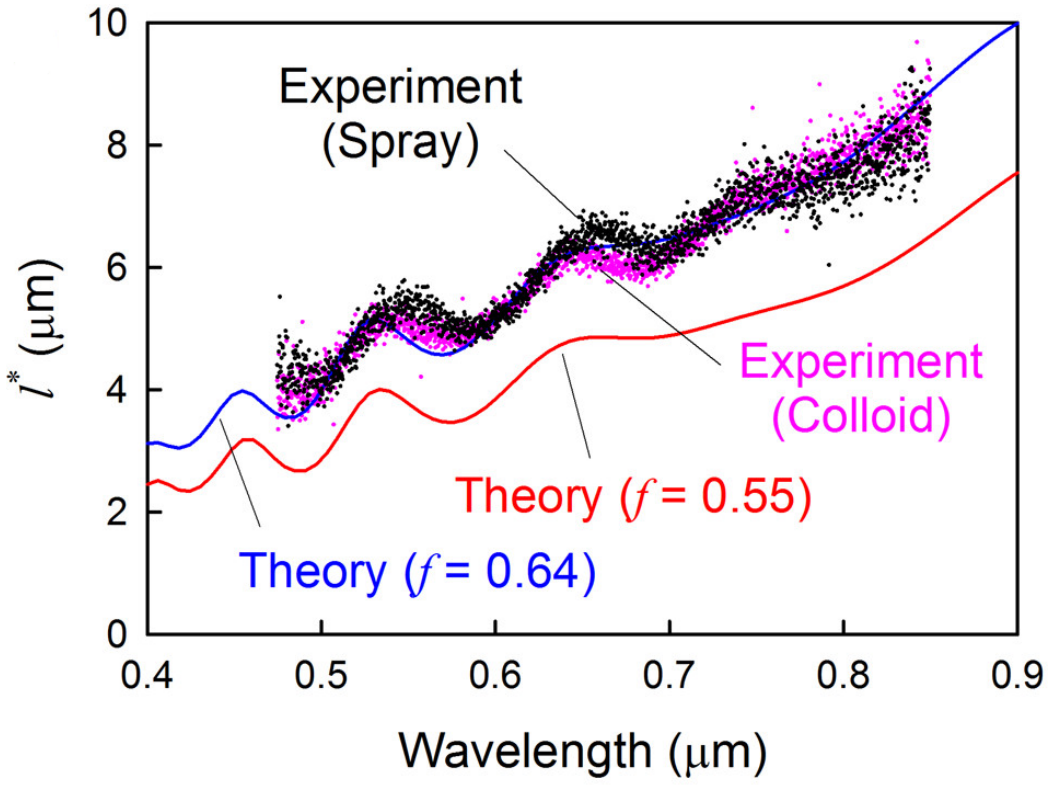

Figure 3.4. Comparison of experimentally measured and theoretically calculated l^* for close (f = 0.64) and loose (f = 0.55) random packing of silica microspheres of d = 0.9 μm. †

While our calculation with the assumed value of the fill fraction of 0.64 accurately described the experimental results, this agreement is not a definite proof that the fill fraction of our samples is 0.64. Our calculation does not fully account for short range ordering [93] and any degree of ordering that might occur in the actual structures would increase l^* due to less efficient scattering. What these imply is that l^* for a fill fraction lower than 0.64 (such as 0.55 as shown in Fig. 3.4) would start to increase from the calculated value shown in Fig. 3.4 in a presence of increasing level of ordering. This increased l^* may match our experimental outcome. In other words, our experimental l^* may correspond to l^* of a sample with a fill fraction lower than 0.64 and some degree of short-range order. Indeed, in a previous study [99], the fill fraction of samples fabricated via colloidal sedimentation method was shown to be approximately 0.55 which corresponds to the lower limit of random loose packing. [98] Since the fill fraction of a structure of randomly packed microspheres is difficult to determine accurately, [101] this work only gives an estimated value of the fill fraction of our samples.

With our experimentally validated theoretical model, the sunlight scattering power, $1/\langle l^* \rangle$, as a function of microsphere diameter and fill fraction, is calculated and plotted in Fig. 3.5. Here, the bracket represents the average value with the solar intensity spectrum as a weighting factor. In Fig. 3.5, the maximum scattering power (region A) is achieved when d = 1.5 μm and f = 0.375, and the maximum $1/\langle l^* \rangle$ is 0.20 μm^{-1}.

Therefore, according to our model, the lowest $\langle l^* \rangle$ is 5.0 μm. On the contrary, in many commercial solar paints, the common sizes of TiO_2 particles (200-250 nm) and hollow spheres (50-150 μm) are very far from the optimum diameter determined for SiO_2 microspheres. While smaller size particles can help reduce the coating thickness and cost, TiO_2 particles have pronounced absorption in UV and near-IR, which compromises their radiative cooling efficiency compared to our coating made of silica microspheres. For large diameter hollow spheres with diameter ranging from 50-150 μm and $f = 0.6$, $l^* = 28$-83 μm. This transport mean free path is much greater than the minimum value of $\langle l^* \rangle = 6.4$ μm that can be obtained for 2-μm-diameter microspheres with the same fill fraction (region B, Fig. 3.5). What this comparison suggests is that the commercial paint made of large hollow spheres must be 4 to 13 times thicker than our SiO_2 microsphere coatings to achieve similar cooling performance.

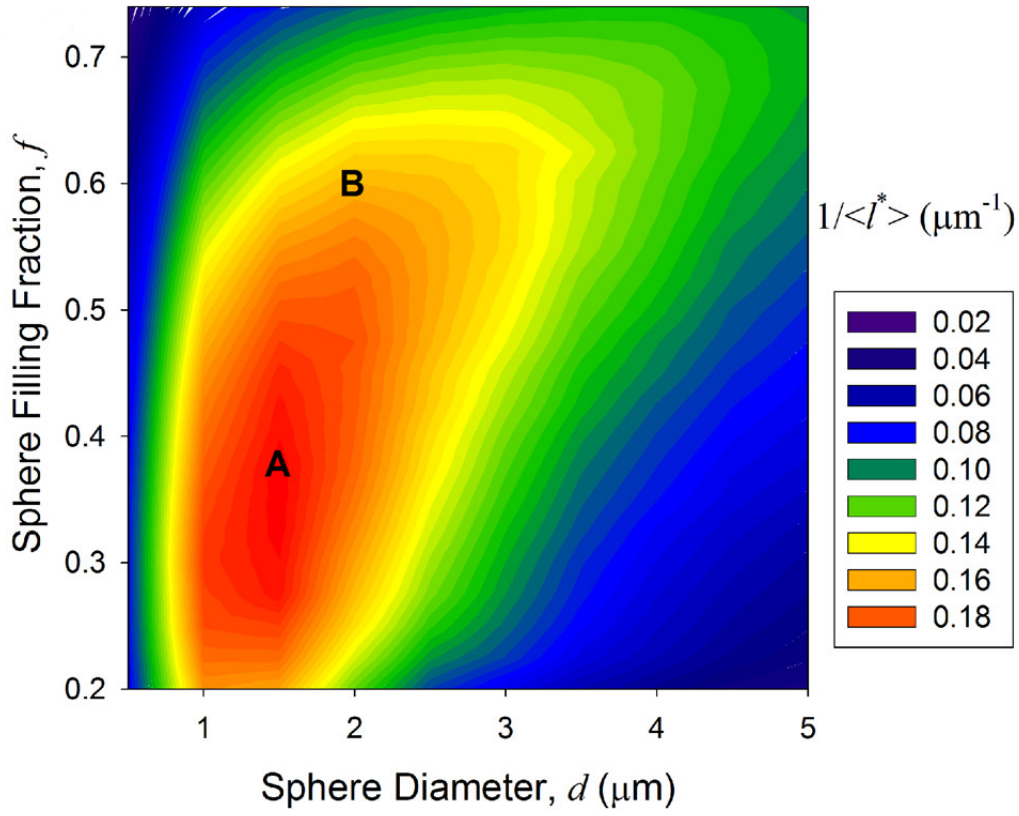

Figure 3.5. Dependence of the solar scattering power, $1/\langle l^* \rangle$, on the sphere diameter and fill fraction of randomly arranged silica microspheres. †

Regarding the fill fraction, $f = 0.55$ is generally considered to be the lower limit in loose random packing of microspheres. Nevertheless Fig. 3.5 shows that the fill fractions much lower than this limit can maximize the scattering power (region A). Thus, the issue is whether or how such low fill fractions can be experimentally achieved. Giera et al. [101] has recently discovered that the fill fraction can be as low as 0.4 when microspheres are subjected to high voltage and driven to sedimentation. At this fill fraction, the light scattering with properly sizes microspheres can be stronger than at the fill fraction above 0.55. For $f < 0.55$, we speculate that the size of air gaps can be larger than individual microspheres and that these gaps are non-uniformly distributed in the

coating. Depending on the scale, the current theory may require modification to accurately model the light scattering in such system.

To estimate the required coating thickness for effective sunlight scattering, we calculate absorptivity as a function of film thickness when the microspheres are coating on an absorbing substrate. Fig. 3.6 shows an example of absorptivity as a function of coating thickness for $d = 2$ μm and $f = 0.6$. We note that these conditions are not optimum for maximum scattering power, but the fill fraction of 0.6 can be easily realized in our current experiment. For this fill fraction, the minimum averaged l^* occurs at the microsphere diameter of 2 μm, which we used for the fabrication. The two curves in Fig. 3.6 represent two extreme values of the internal reflectance, R_s, at the coating-substrate interface. The two cases, $R_s = 0$ and $R_s = 0.96$, correspond to an ideal black body and a highly reflective metal as a substrate respectively. The difference in absorptivity becomes smaller as the coating thickness increases, because the reflection from the coating becomes dominant as its thickness increases. For samples made of 2-μm-diameter silica microspheres with $f = 0.6$, the absorptivity is less than 3% as the coating thickness reaches 500 μm. At this low absorptivity, previous works [57,58,60] achieved substrate cooling 5-10 °C below the ambient temperature. In this work, we will show that we can achieve a similar performance with silica coatings and without expensive metal coating.

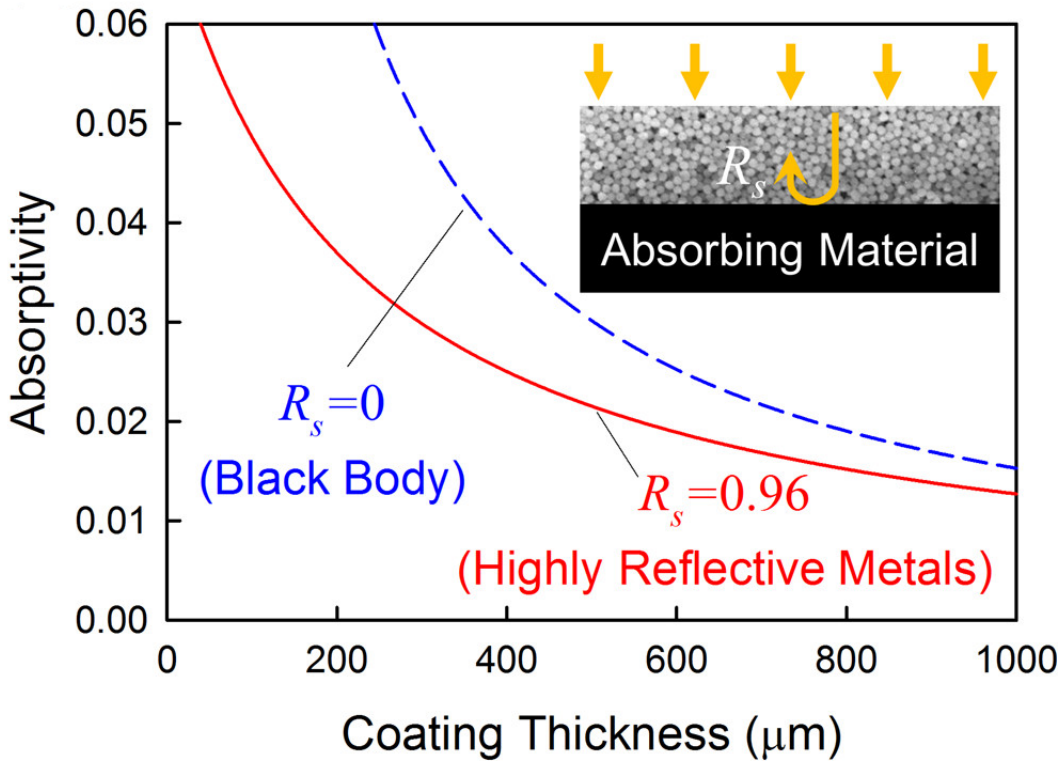

Figure 3.6. Absorption of a substrate with a microsphere-based coating for d = 2 μm and f = 0.6 as a function of coating thickness for two extreme values of internal reflectance R_s at the coating-substrate interface. †

The mean field theory that we use for theoretical calculations does not take into account the correlations of microsphere positions except for short-range correlations induced by the sphere size. In practice, the short-range correlations may be stronger than the theoretical approximation and will depend on the microsphere deposition techniques and parameters. In a presence of strong correlations, experimentally determined l^* may deviate from the mean field theory calculation. To study the impact of short-range correlations on l^*, we compared coatings of randomly packed 2-μm-diameter microspheres, fabricated by the spray coating method at different surfactant concentrations.

Fig 3.7 (a)-(c) shows scanning electron micrographs of the top surface of the microsphere coatings prepared with different surfactant concentrations. From these images, the microsphere arrangement appears to be quite random. Following the method described by Garcia et al. [46], we calculate autocorrelation functions from the images and confirm the randomness. The 2D autocorrelation functions are circularly symmetric which implies that the random arrangement is isotropic. The value of autocorrelation functions shows the maximum at the center and decay sharply along the line radially extending from the center. This behavior corresponds to a random microsphere arrangement (which is naturally isotropic). The functions also show small peaks approximately at integer multiples of d. These peaks correspond to short-ranged correlations that are present because of the nonzero size of the microspheres. [46] Because contrast and brightness in the SEM images vary from sample to sample and depend on many parameters, it is difficult to quantitatively compare the autocorrelation functions and evaluate the degree of randomness in the three samples.

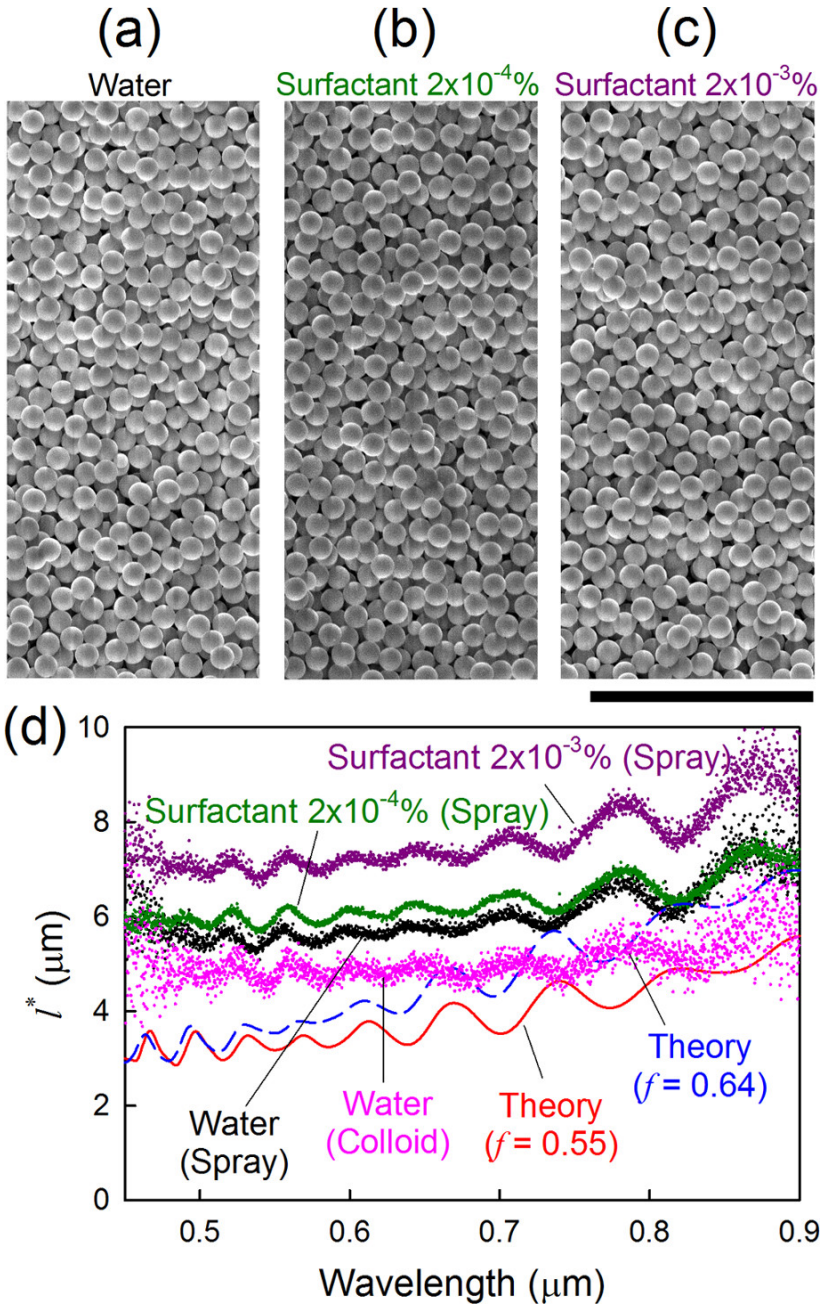

Figure 3.7. (a-c) SEM images of silica microspheres of d = 2 μm deposited by spray coating when the surfactant concentration is (a) 0%, (b) 2×10^{-4} %, and (c) 2×10^{-3} %. The scale bar represents 20 μm. (d) l^* spectrum for the three cases and the sample prepared by colloidal deposition. Theoretical predictions for close (f = 0.64) and loose (f = 0.55) random packing of silica microspheres are also shown in comparison in (d). [†]

Because of the difficulty with comparing the autocorrelation functions, we measured the l^* of the samples for comparison instead. As shown in Fig. 3.7 (d), l^* for spray-coated samples increases as the surfactant concentration increases. In the visible spectrum, l^* increases by 1.7 μm when 2×10^{-3} volume % of surfactant is added, compared to the l^* of the sample without any added surfactant. We also observe that the spray-coated sample without surfactant exhibits l^* that is larger than that of the sample prepared by colloidal sedimentation method. While the spray coating method is a more convenient technique that the sedimentation method, the shorter l^* for sediment sample implies that the sedimented microspheres are more randomly distributed or their fill fraction is lower than the spray-coated microspheres. However, in all cases, the measured l^* shows deviations from theoretical predictions for both $f = 0.55$ and $f = 0.64$. This comparison with the theory suggests that, while the sphere arrangement shown in the SEM images appears random, the surface images alone cannot quantitatively represent the optical scattering strength in the bulk.

ii) Emissivity spectrum

In Fig. 3.8, the emissivity spectrum (green) from the microsphere coatings is plotted against solar (red) and atmosphere (blue) radiation intensity. The emissivity, which is equivalent to absorptivity, of the sample is negligible in most of the solar radiation spectral range (0.3-3 μm). On the contrary, the emissivity is high in the atmospheric transparency window (8-13 μm) highlighted in orange. Emissivity peaks in the near IR (1.9-3 μm) are due to intrinsic absorption of SiO_2 and correspond to a less than 0.1% increase in the solar absorptivity. The average IR emissivity of this coating over the atmospheric transparency window is greater than 0.94, which is greater than that

in reference [59] where 8-μm-diameter microspheres were used. The reason for the high emissivity in our random media is that our porous media provides better optical impedance matching with the air, compared to the case of a solid silica film. According to Maxwell-Garnett effective medium theory [102], we estimate that the average emissivity in the normal direction over the atmospheric transparency window for our media with a fill fraction of 0.55 would be greater than that of a solid silica film by more than 0.13.

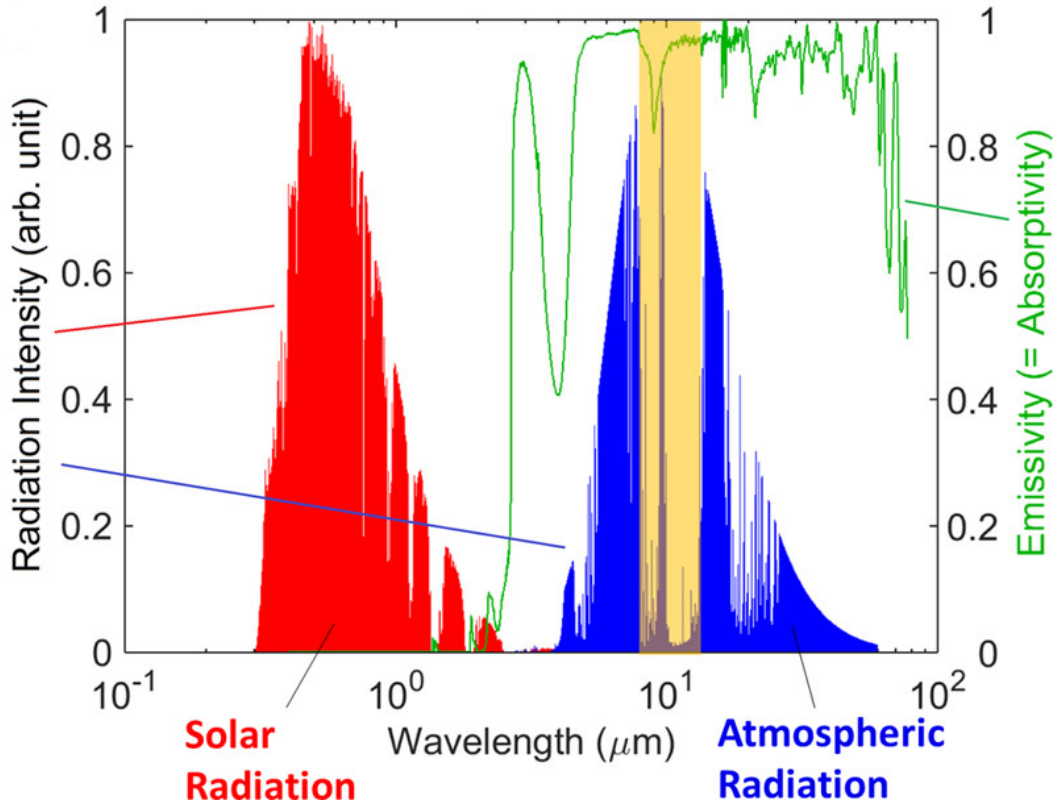

Figure 3.8. Experimentally measured emissivity spectrum of randomly packed silica microspheres (green) against solar (red) and atmospheric (blue) radiation intensity. †

The high emissivity outside the atmospheric transparency window decreases the cooling performance [72]. However, this effect is significant only when heat transfer by

convection and conduction from the ambient air is negligible [60,103]. Because the coating for outdoor radiative cooling would be exposed to the ambient air in many common applications, the convection and conduction of heat is substantial, and the high emissivity of our coating outside the window would not strongly affect the cooling performance. In fact, this high emissivity outside the window is actually desirable for cooling when the coating temperature is higher than the ambient air temperature.

iii) Outdoor temperature measurement and cooling performance comparison

The results from our outdoor temperature measurement is shown in Figure 3.9. In the figure, our microsphere coating on a black substrate, without the use of expensive silver coatings, can reduce the substrate temperature below that of the ambient air by as much as 12 °C under the sunlight. Our coating also outperforms the commercial solar-reflective white paint. At its peak performance, our coating achieves a substrate temperature 7 °C below that of the commercial paint. The average temperature of the substrate under our coating is 4.7 °C below that of the substrate coated with the commercial paint during the time of strong solar radiation (11am – 4pm). At night (9 pm - 7am), both microsphere and commercial paint both maintain the substrate temperature 4 °C below the ambient. This result suggests that both films have similar radiative properties in the mid-IR, but our microspheres coating has better scattering properties for the solar radiation than the commercial paint.

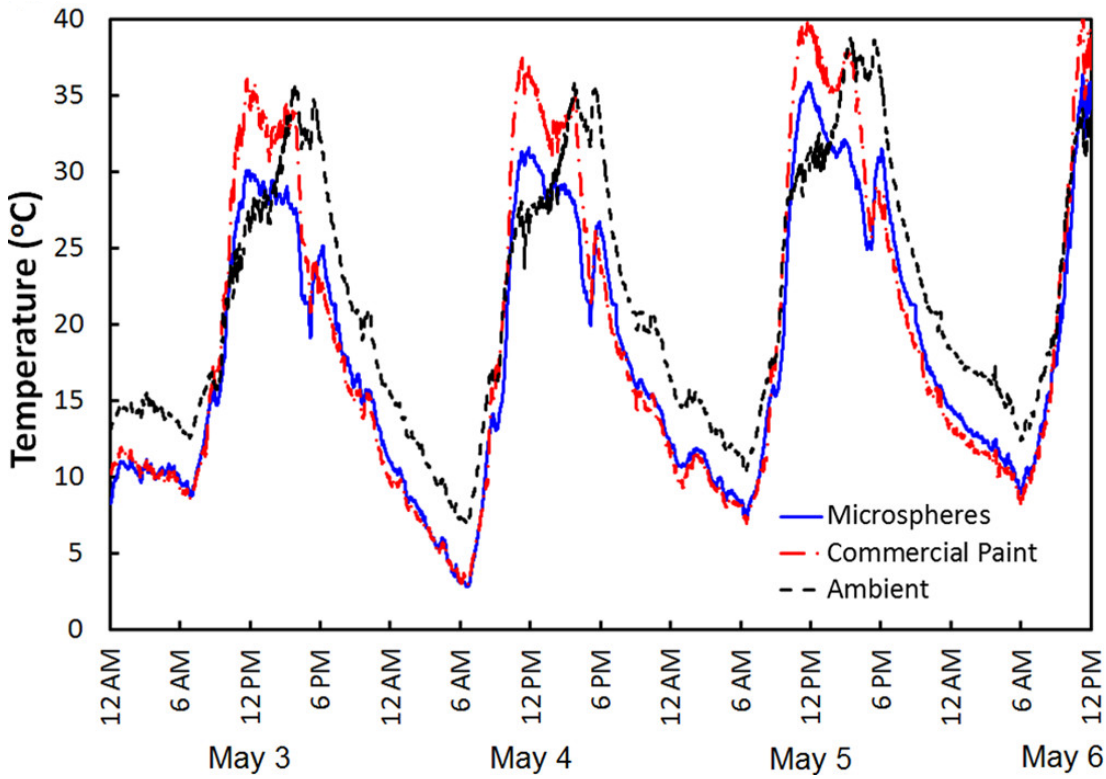

Figure 3.9. Measured temperature variation over 3.5 days for our microsphere sample, commercial white paint, and ambient air. †

We also observe that substrate temperatures of microsphere coating and commercial paint both increase faster than that of the ambient air from 7 am to 12 pm. The reason is that the solar absorptivity of the solid coatings is still higher than that of the ambient air, even though the absorptivity in the substrate is approximately 0.02. From 7 pm, when the sun's altitude is lower than 10°, until 7 am, the substrate temperature starts to decrease before the ambient temperature does with a time lag of 1-2 hours. During this time, the solar heating is negligible, and the substrate is cooled by radiation in the mid-IR. The radiative cooling of the sample is stronger than that of the ambient air, and thus the substrate temperature decreases below the ambient temperature.

3.6 Conclusion

In this chapter, we have shown that the random media comprised of silica microspheres can achieve strong radiative cooling under direct sunlight. This excellent performance is achieved with coatings where microsphere size and fill fraction are not yet fully optimized, and thus there is a strong potential to further improve its cooling performance. Our coating cools a black substrate below the ambient temperature by as much as 12 °C. On average, our coating also reduces the substrate temperature 4.7 °C below that of the commercial white paint during the period of strong solar radiation. Unlike other radiative cooling technologies that employ costly fabrication methods or expensive materials, our coatings are created with facile and scalable methods with a very low cost. We also note that, because our coatings are in a paint format, pigments can be easily incorporated for aesthetic and commercial purposes. Furthermore, in this study, we show that the optical scattering power can be maximized with appropriate choice of microsphere size, material, and fill fraction. We also note that the optimal parameters of random structures significantly differ from those in current commercial products. Therefore, our study offers a path toward low-cost coatings with substantially improved radiative cooling performance. In future works, we aim to investigate the fascinating ability of random media to separately control optical properties at different spectral bands. Such ability could have strong implication on other applications such as infrared sensors, water harvesting and purification, and thermal management in fabrics. For practical applications, works to improve durability and antisoiling properties would also be beneficial.

Portions of this chapter have been published as S. Atiganyanun, J. B. Plumley, S. J. Han, K. Hsu, J. Cytrynbaum, T. L. Peng, S. M. Han, and S. E. Han, ACS Photonics **5**, 1181 (2018) and are reproduced with permission of the publisher.

[†]Figure reproduced with permission from S. Atiganyanun, J. B. Plumley, S. J. Han, K. Hsu, J. Cytrynbaum, T. L. Peng, S. M. Han, and S. E. Han, ACS Photonics **5**, 1181 (2018).

Chapter 4: Radiative Cooling with Disordered Hollow Microsphere-Based Structures

*Reproduced in part with permission from J. D. Alden, S. Atiganyanun, R. Vanderburg, S. H. Lee, J. B. Plumley, O. K. Abudayyeh, S. M. Han, and S. E. Han, Journal of Photonics for Energy **9**(3), 032705 (2019). DOI: 10.1117/1.JPE.9.032705.

4.1 Overview

In the previous chapter, we have demonstrated that the paint-format materials of randomly packed monodisperse SiO_2 solid microspheres can improve solar scattering efficiency dramatically by optimizing the size, fill fraction, and packing arrangement of microspheres. Under the intense solar radiation, these coatings can decrease the underlying substrate temperature by as much as 12°C. The observed temperature was also below the temperature of substrates coated with leading commercial solar-reflective paint by an average of 5°C. Unlike other cooling technologies employed in recent works, [57–60] our coatings do not require precious metals such as silver or expensive processing steps such as metal deposition in vacuum.

Nevertheless, there are some improvements from our work that can be explored. First, we note that the sphere size and the fill fraction of the silica coatings are not yet fully optimized. Specifically, our calculation has shown that decreasing the fill fraction would increase the light scattering power (in solar region) further. However, it is currently difficult to decrease the fill fraction of randomly arranged solid monodisperse microspheres below 0.55, which is considered a theoretical lower limit. Therefore, to

decrease the solid fill fraction of such structures, we employ hollow polymer microspheres instead of solid silica microspheres for fabrication of the disorder structures. We will show that the coatings that consist of the hollow polymer microspheres achieve stronger light scattering than those that consist of the solid microspheres.

Second, our previous structures do not possess mechanical durability compared to commercial paints. This is due to the fact that, in our coatings, microspheres are merely touching and their surrounding matrix is air. To address this issue, we can slightly merge the hollow polymer microspheres to improve slightly mechanical strength without affecting the optical properties. However, even after merging, the mechanical properties are still far from those of commercial paints. To fully address this problem, we mix the polymer hollow microspheres with silicone. The continuous silicone network significantly enhances mechanical durability over the randomly packed solid microspheres in our previous work. In terms of optical properties, silicone reduces near-IR absorptance to a value less than conventional acrylic polymers in most paint binders, and the hollow microspheres eliminate ultraviolet (UV) absorption of TiO_2 particles in commercial paint. Because the hollow microspheres and silicone are inexpensive material, the coating thickness is not a significant economic concern. The coatings can be thick enough to achieve efficient radiative cooling without the need for fully optimizing the microsphere arrangement. The coatings can also be conveniently applied on any surface. Additionally, silicone is a space-flight-qualified material, and thus the coating has potential for radiative cooling in space environment. [104]

4.2 Optical properties

The physics behind light propagation in random media is similar to that described in the previous chapter. In summary, one important parameter in the diffusion model in light transport in random media is the transport mean free path (l^*). The length is defined as the average distance that a photon energy packet travels before its propagation direction no longer correlates with its original direction. In general, l^* depends on the wavelength λ. This length also relates total transmittance and thickness of a random medium:

$$T = \frac{1 + z_e}{L / l^* + 2z_e}, \tag{4-1}$$

where z_e is the extrapolation length normalized by l^*, and the extrapolation length is the distance outside the film over which the diffuse light intensity approaches zero. [89,90] From Eq. (4-1), if a random medium is placed on a black substrate, the total transmittance can be replaced by absorptance A. Therefore, the goal is to minimize $1/l^*$ to achieve the lowest absorptance.

In our previous chapter, we have shown that l^* spectrum can be accurately calculated by the mean field theory [92,93] for solid microspheres. With the theoretical model that has been experimentally verified in our previous work, [105] we calculate sunlight scattering power, $1/\langle l^* \rangle$, for randomly positioned spherical bubbles in a matrix of refractive index n = 1.5. Here, $\langle\ \rangle$ represents the average value with the solar intensity spectrum as a weighting factor.

4.3 Experimental methods

i) Hollow microsphere film

The hollow microspheres (ROPAQUE^{TM} AF-1055, Dow Chemical Co.) consist of a shell made of polystyrene-polymethyl methacrylate copolymer. The inner and outer diameters of the hollow are 0.82 and 1.0 μm, respectively. To measure the refractive index of the polymer shell, we dispersed the hollow microspheres in an aqueous solution of zinc iodide at varying concentrations.[106] When the specular transmittance is maximized, the refractive index is matched between the microsphere shell and the liquid mixture. The refractive index of the shell is determined to be 1.504 at a wavelength λ = 632.8 nm.

We employ the spray coating method (similar to that in Chapter 3) to create coatings that consist of randomly arranged polymer microspheres. A solution of the hollow microsphere in pure isopropanol (IPA) was prepared. The volume fraction of the hollow spheres was 2%. Here, we use IPA as a dispersing medium instead of water as in the previous work to increase evaporation rate during spray coating. Because the hollow microspheres have lower glass transition temperature (~80 °C) than that of solid silica microspheres (≥ 800 °C), heated substrate temperature cannot be set as high as in the previous work during the deposition. Therefore, we select IPA due to its high vapor pressure to compensate for lower substrate temperature. The solution was ejected through an air-brush nozzle (Badger 100G, Badger Air-Brush) at 69 kPa. The nozzle was located 22.5 cm above a glass substrate. The substrate was subjected to a linear periodic motion and was heated at ~50 °C. The thickness can be controlled by the total amount of the solution volume that is dispersed. For l^* measurement, the thickness of coatings ranged

from 20-100 μm. For outdoor temperature measurement, the thickness was ~300 μm and the substrates were 6061 aluminum alloy wafers. This alloy is a commonly used material for roofing sheets and frames. For comparison, samples coated with a commercial paint (Spartacryl PM 60312, Chromaflo Technologies) of the same thickness on the alloy wafers were also prepared.

To study effects of thermal merging of the hollow spheres, we heated the hollow sphere samples at 78 °C, using a furnace tube (TF55030A-1 Lindberg/Blue M, Thermo Scientific). After undergoing the heating, top surfaces of the samples were characterized with a scanning electron microscope (FEI Q3D FIB/SEM DualBeam system, ThermoFisher Scientific).

To characterize the coating optical properties, we measured the total transmittance in the solar wavelength region of the media with an integrating sphere (ISO-50-8R, Ocean optics) connected to a photospectrometer (USB4000-VIS-NIR, Ocean Optics). The thickness, needed for l^* calculation, was measured by the scanning electron microscope The optical properties of our samples and commercial paints in IR wavelength were also measured with spectrophotometers with integrating spheres (Lambda 950, PerkinElmer for $\lambda = 0.2 – 2.5$ μm and INVENIO R, Bruker for $\lambda = 2.5 – 50$ μm).

For characterization of cooling performances, four samples with the 6061 aluminum alloy substrates were prepared: two with our coatings and two with the commercial coatings. We built a very simple setup that simulates a common usage of commercial paints exposed to the ambient environment (Fig. 4.1). In this setup, a thermocouple was attached to the backside of each sample. The samples were placed on a

large Styrofoam block of thickness 0.75 inches, which reduced the heat conduction from the floor. Before the setup was moved to a rooftop where the actual temperature measurement occurs, the samples were cover by another Styrofoam block, placed ~1 cm above the coatings. The setup was then moved to the rooftop of a building, the cover was removed, and the sample temperatures were measured for continuous 1.5 days in November in Albuquerque, NM.

Figure 4.1. Optical image of our setup for outdoor temperature measurement. The left and right samples are a square substrate coated with the hollow microspheres and the commercial paint respectively. The width of the substrate is 4 inches.

ii) Hollow microspheres in silicone matrix

To create random media consisting of the hollow microspheres embedded in silicone matrix, we mixed the same hollow microspheres (also called microbubbles in this work) with silicone monomers (ELASTOSIL® RT 601, Wacker Chemie AG). The silicone monomers were hardened by adding a platinum-based cross-linker catalyst to

form polydimethylsiloxane. The volume fraction of the hollow microspheres was 23%. Solutions of higher volume fractions require vigorous mixing due to increased viscosity. These films were then coated on a side of glass slides over a 1 in. × 1 in. area with a thickness of 2 mm. The other side of the substrates was painted black (Specialty Black High Heat Ultra, Rust-Oleum). The absorption of the black paint was measured to be 0.97 in the visible spectrum. For comparison, samples coated with a commercial paint (Spartacryl PM 60312, Chromaflo Technologies) of the same thickness on the similar black-painted glass slides were also prepared.

The mechanical durability of these silicone coatings was tested by placing the samples inside a high vacuum chamber. The reflectance spectra of our sample, commercial paint, and 6061 aluminum alloy were measured by spectrophotometers with integrating spheres (Lambda 950, PerkinElmer for λ = 0.2 – 2.5 μm and INVENIO R, Bruker for λ = 2.5 – 50 μm). The thickness of our sample and the commercial paint was identical at 2 mm. Due to systematic errors in an integrating sphere measurement, [107–109] we employed another setup comprised of an integrating sphere (ISP-50-8R, Ocean Optics) coupled to a detector operating mostly in the visible range (USB4000-VIS-NIR, Ocean Optics) and made error corrections to the measured reflectance using the procedures described in the appendix B.

To quantify temperature rise due to absorption in the solar spectrum alone, we illuminated the samples by a solar simulator beam of AM1.5G spectrum (ABET Technologies, 1050), measured their temperatures, and compared them to the ambient temperature [Fig. 4.2]. Each sample was placed in a box (29 cm × 29 cm × 3.7 cm) made with an optically transparent, low-density polyethylene (LDPE) film wrapped around a

wood frame. The LDPE box provided a controlled thermal environment with a constant heat transfer coefficient to the surroundings. The ambient temperature was measured inside the box near its corner far from the illumination area. Thermocouples were attached to the bottom surface of the samples. We measured the temperatures of our samples, commercial paints, and a block of 6061 aluminum alloy.

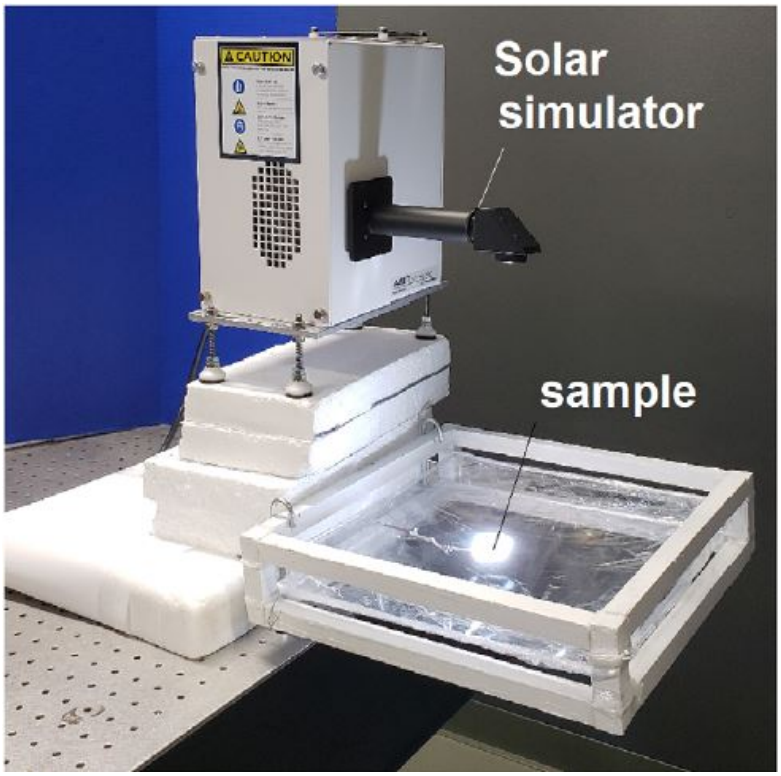

Figure 4.2. Optical image of experimental setup for temperature measurement with a solar simulator. The incident solar simulator beam is AM1.5G spectrum. The sample area is 1 in. × 1 in for all the samples, and the light beam covers the entire sample area. †

To evaluate the cooling performance of the hollow microspheres-in-silicone coatings under the sky with exposure to actual sunlight, we prepared a fixture as shown in Fig. 4.3. We measured the temperature of a substrate coated with our hollow microspheres-embedded silicone, a substrate coated with commercial paint, and the

ambient air in Albuquerque, New Mexico on September 4, 2018. The sky was partly cloudy for the day. The samples and the ambient probe were located ~2m above the rooftop so that the temperatures were not strongly affected by the heated rooftop surface. The two samples were enclosed in two separate but identical LDPE boxes.

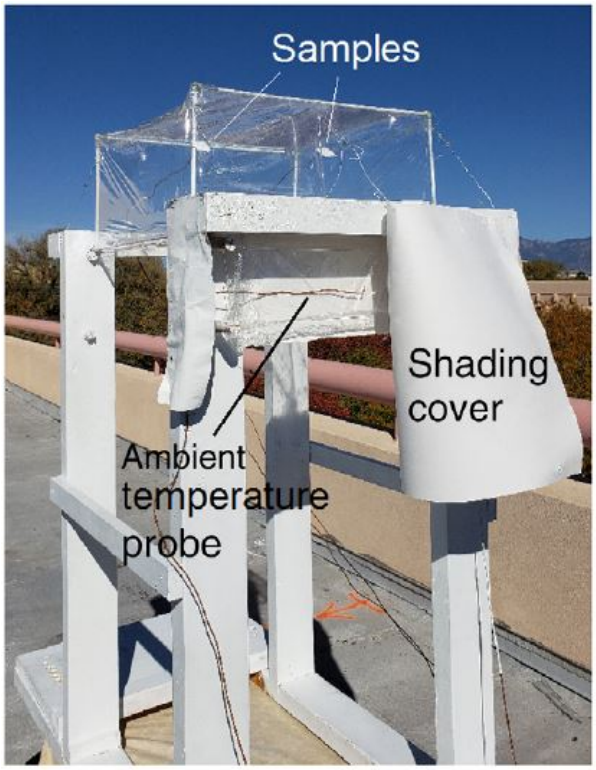

Figure 4.3. Optical image of our outdoor experiment setup for temperature measurements. The white shading paper covers the ambient temperature probe for the experiment is partially peeled open to illustrate the probe. †

4.4 Results and discussion

i) Hollow microsphere film

Scanning electron micrographs of merged hollow spheres are shown in Fig. 4.4. We observe that some hollow microspheres are partially merged when subjected to heating at 78 °C for 15 minutes (Fig. 4.4 (a)). However, when the thermal treatment is extended to 1 hour (Fig. 4.4 (b)), some hollow microspheres are deformed, showing the inner void. We speculate that, at the lower duration of heat treatment, the polymer only on the outer surface of the shells acts like a liquid and forms connected bridges between two or more microspheres. However, at a longer heat treatment, the polymer on the inner surface of the shell begins to flow as well and causes collapse of the shell structures, leading to the deformation. Therefore, the duration of heat treatment must be carefully chosen to achieve merging of the microspheres and avoid the collapse of their structures.

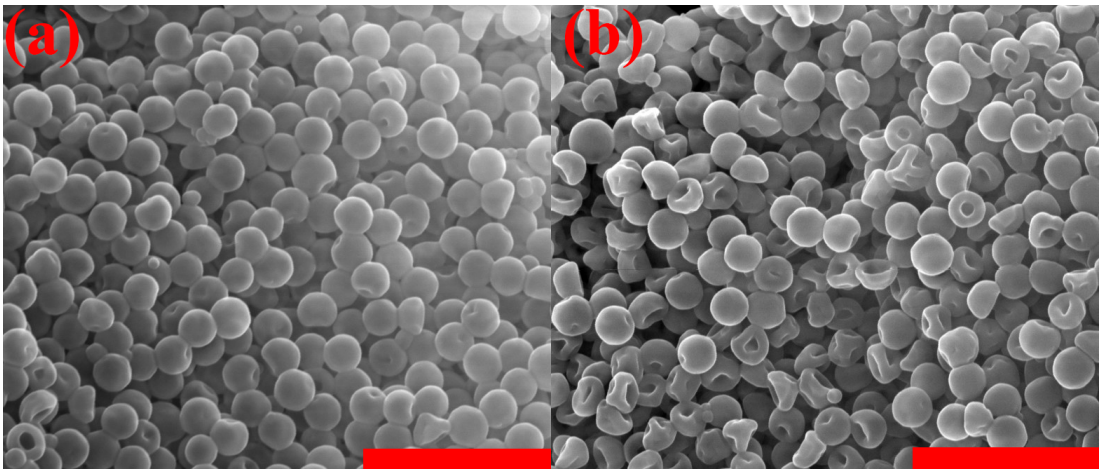

Figure 4.4. Scanning electron micrographs of the hollow polymer microspheres subjected to a thermal treatment at 78 °C for (a) 15 minutes and (b) 1 hour. Merging between the particles occurs at both condition, but the microspheres are severely deformed in (b). The scale bar represents 5 μm.

The transport mean free path of the hollow microsphere coatings (red dots) compared to that of the 0.9-μm-diameter silica microsphere coatings studied in Chapter 3

(black dots) is shown in Fig. 4.5. l^* of the polymer coatings has been reduced by half from l^* of the silica coatings in the solar spectrum. This indicates that the scattering efficiency in the solar region of our samples consisting of hollow microspheres increases by ~100% from that in our previous work. This is indeed a significant improvement. This change also agrees with our hypothesis that, by lowering the solid fill fraction of our random media via usage of hollow microspheres, l^* would decrease.

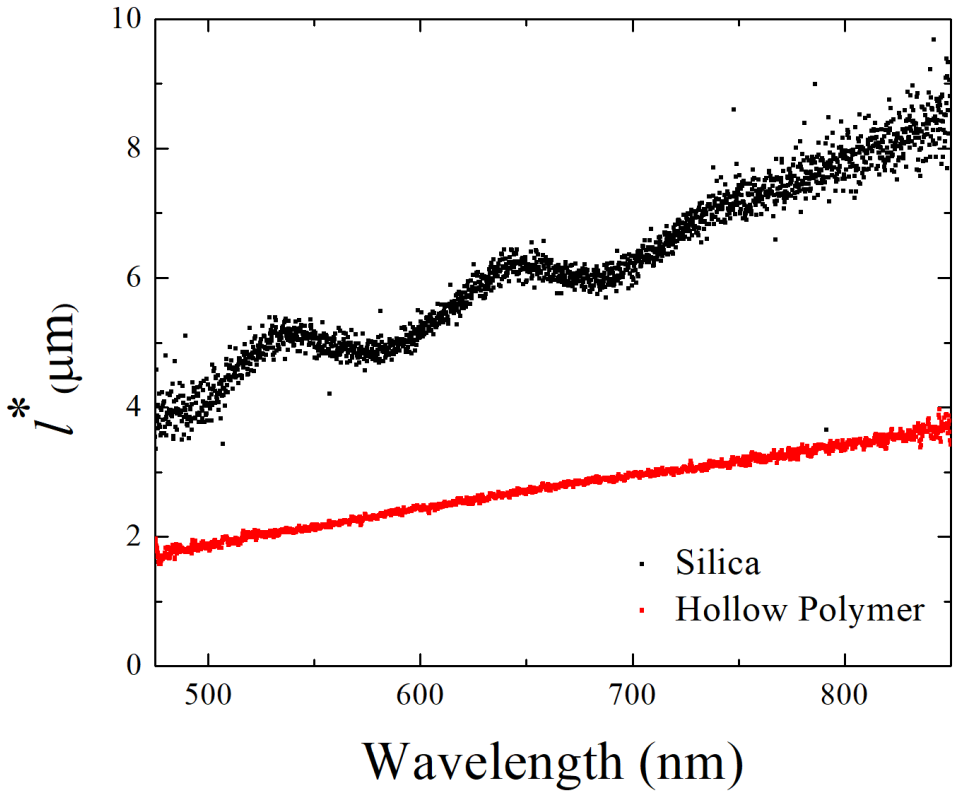

Figure 4.5. Transport mean free path of the disordered coatings that consist of solid silica microspheres (black dots) or polymer hollow microspheres (red dots) as a function of wavelength.

Unlike the case of the silica microspheres, l^* in the hollow polymer microsphere coatings do not exhibit resonance behavior, which would appear as bumps and trenches.

The lack in resonance is due to the air gap inside the hollow microspheres. In the solid microsphere structures, the resonance occurs inside the solid microspheres, which have higher refractive index than the surrounding matrix. Since, the diameter of the solid sphere matches with the optical wavelength, the resonance can be confined in the microspheres and occur in the solar regime. On the contrary, the high-refractive index material only exists inside the shells, in the case of the hollow microspheres. The shell only has thickness of 90 nm and thus cannot confine the light in the solar spectrum. Therefore, the resonance in the hollow microsphere is not observed.

Measured emissivity spectrum for the polymer hollow microspheres and the commercial paint is shown Fig. 4.6(a) for λ = 0.35 – 4 μm and (b) for λ = 4 – 40 μm. In the solar spectrum, our polymer hollow microsphere structures have lower emissivity than that of the commercial paint. This is beneficial for solar rejecting performance. At equilibrium, emissivity must be equal to absorptivity at a wavelength. Therefore, the hollow microsphere coatings absorb the solar radiation less than the commercial paint and thus are expected to perform better during daytime.

In the IR spectrum (Fig. 4.6(b)) above 4 μm, we observe that the emissivity of the hollow microsphere samples is higher than that of the commercial paint except for λ = 8-13 μm. Because this particular wavelength range corresponds to the atmospheric transparency window, this suggests that the commercial paint will lose heat more efficiently during the nighttime and when the substrate temperature is below the ambient temperature. Therefore, there is still some room for improvement in the hollow microsphere coating technology. In our previous work in Chapter 3, we demonstrated that solid silica microsphere coating maintain high emissivity in the transparency window due

to the intrinsic properties of silica itself and due to enhanced impedance matching. Therefore, we speculate that if hollow microspheres are made of silica itself rather than the PS-PMMA copolymer, emissivity in the transparency window can be improved.

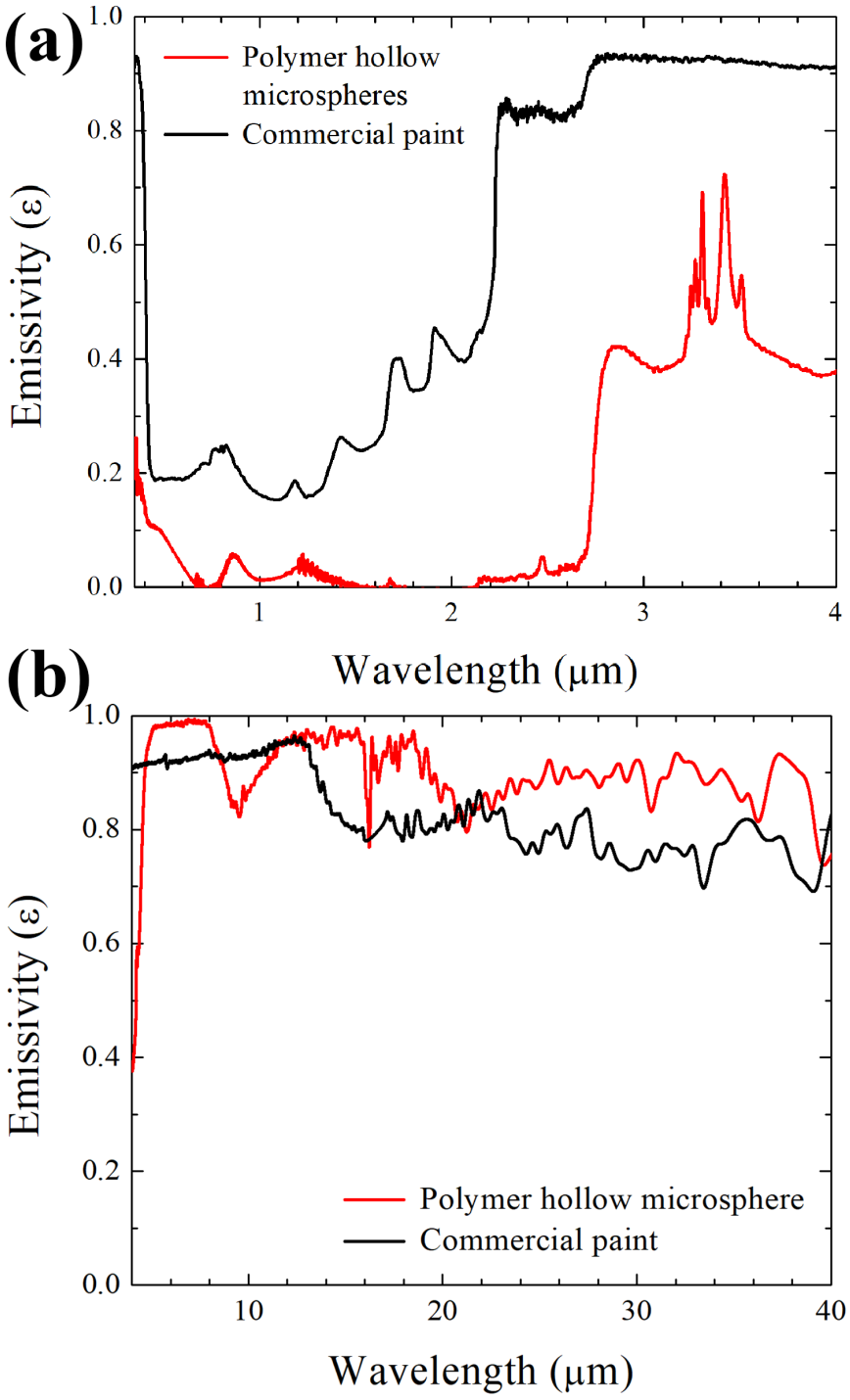

Figure 4.6. Emissivity at (a) λ = 0.35 – 4 μm and (b) λ = 4 – 40 μm of the polymer hollow microsphere coatings (red line) and the commercial paint (black line)

The measured temperature variation over time for both samples is shown in Fig. 4.7. At the beginning of the measurement, the temperature of both samples decreases sharply as they are moved from inside a building (T~21 °C) to the outdoor (T~12 °C). This precipitous drop in temperature is due to the heat convection and conduction overwhelming radiative heat transfer. Around 10 am, effects of radiative heat transfer become dominant. It is observed that the temperature of the substrate coated with the hollow microspheres is ~2 °C lower than that of the substrate coated with the commercial paint on average during times where the solar radiation is strong (11am-3pm). This trend agrees with both measured l^* and emissivity values in the solar spectrum. Because our hollow sphere structures have shorter l^* and smaller emissivity in the solar region, the structures scatter incident solar radiation more efficiently and also absorb it less. Compared to the cooling performance of silica microsphere-based structures in Chapter 3, the daytime cooling performance of our hollow microsphere-based sample seems to be weaker. This is likely due to the fact that solar radiation during fall where the temperature measurement in this work took place is significantly smaller than that during the summer.

During the night, the temperature of the substrate coated with the hollow microspheres is ~3 °C higher than that of the substrate coated with the commercial paint. This result is also expected because our emissivity measurement shows that the commercial paint has higher emissivity in the transparency windows and therefore can lose more heat via mid-IR radiation. This disadvantage of our hollow microsphere paints can be addressed in two ways. One aforementioned way is to use hollow microspheres

made of silica instead of the polymer. The other way is explored in another part of this chapter where our polymer microspheres are embedded within silicone, which is a material with high emissivity in the transparency window.

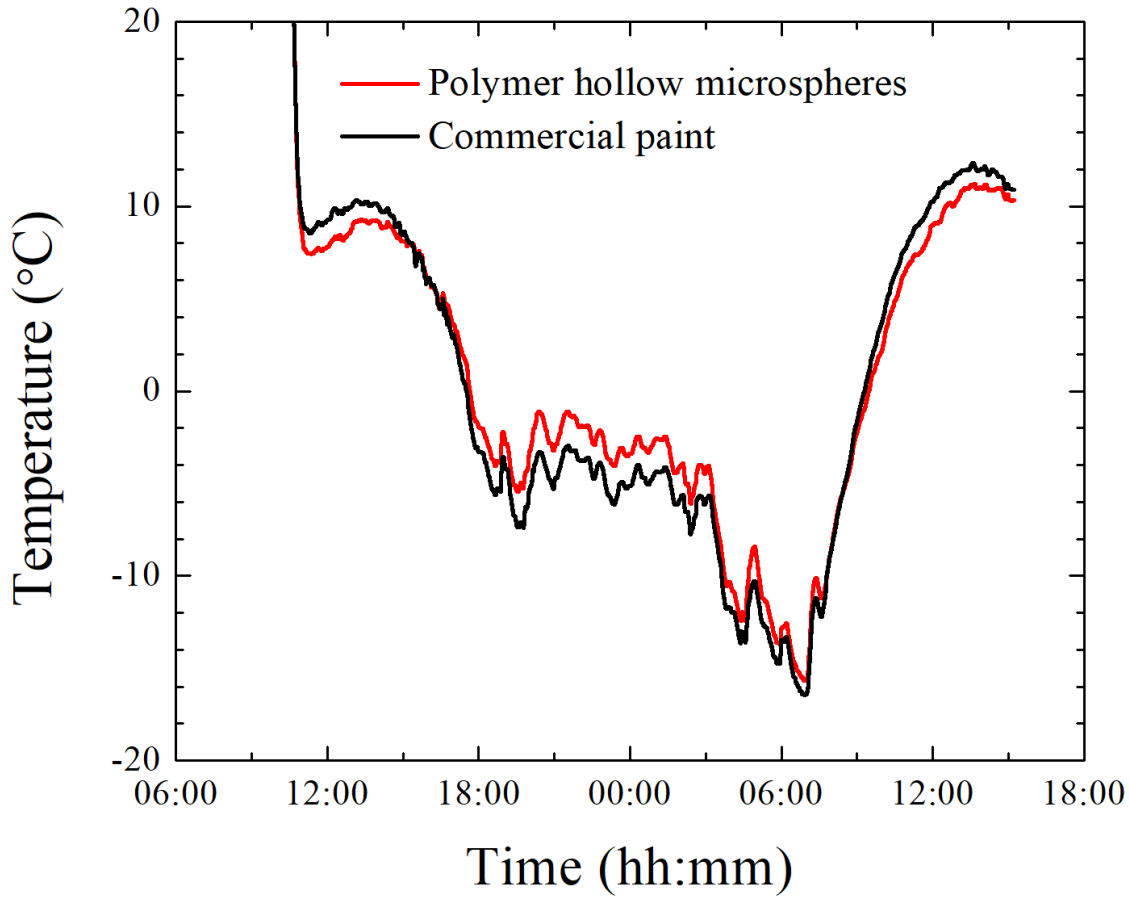

Figure 4.7. Measured temperature variation over a 1.5 days for the hollow microsphere sample and the commercial paint sample, exposed to the ambient air.

ii) Hollow microspheres in silicone matrix

Results from the mean field theory calculation are shown in Fig. 4.8 as a function dimensionless inner sphere diameter, $\langle nkd \rangle$, and fill fraction f. Here, $k = 2\pi / d$ is the magnitude of the free-space wavevector and d is diameter of the spheres. The figure

shows that the sunlight scattering power can be maximized by selecting appropriate size of the hollow microspheres and fill fraction (red region). Commercially available hollow spheres are commonly made of low-refractive index materials and their size ranges from 45-150 μm, [73] which is very far from the optimal conditions. While our hollow microspheres are not at the optimum, the calculated sunlight scattering power of our coatings far exceeds that of commercial paint with hollow spheres. Indeed, from the calculation, the commercial paint made of hollow spheres must be 3 to 18 times thicker that our hollow microsphere-based film to achieve similar scattering performance.

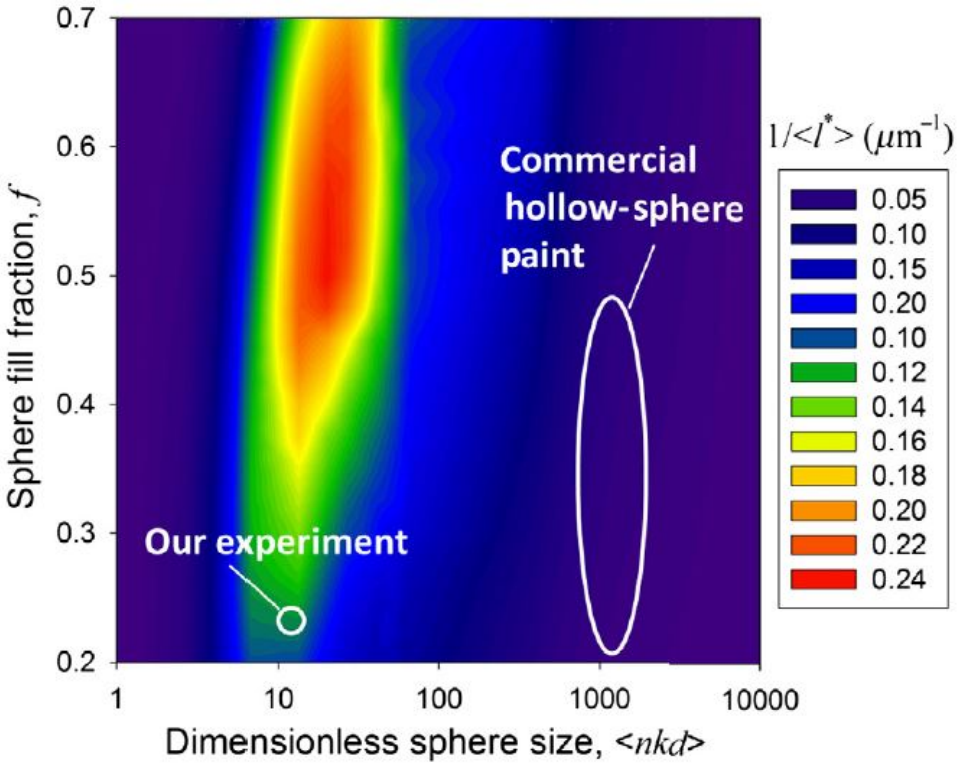

Figure 4.8. Dependence of sunblock power, $1/\langle l^* \rangle$, on dimensionless diameter and fill fraction of randomly distributed hollow microspheres in a medium of refractive index n = 1.5.[†]

When placed in vacuum, the hollow microspheres in the silicone matrix do not rupture, and the coating maintains its mechanical integrity. This suggests that, if the polymer-based hollow microspheres are replaced by radiation-resistance materials, such as silica hollow spheres, the coatings are likely to be qualified for extraterrestrial applications. Indeed, the pseudomorphic glass comprised of silica and silicone has already been tested for space voltaics, and thus this material combination strongly supports the potential space application of our coating. [110,111]

Measured reflectance spectra of our sample, commercial paint, and 6061 aluminum alloy are shown in Fig. 4.9. Our sample exhibits a slightly higher reflectance than the commercial paint over the visible spectrum. In contrast, the difference in reflectance is more significant in UV and near-IR region. The commercial paint is based on TiO_2 particles, and their string UV absorption is detrimental to the cooling efficiency under the sunlight. The strong near-IR absorption of the commercial paint is due to the amplified absorption in the polymer matrix by scattering. [112] Silicone is intrinsically less absorptive in near-IR than polymers in commercial paint products and shows superior performance in solar reflection. The aluminum alloy has a significantly lower reflectance over $0.3\ \mu m \leq \lambda \leq 1.4\ \mu m$ than our sample. This indicates that the silicone-based with embedded hollow microspheres would be highly effective in rejecting sunlight when applied on metal roofing sheets. Based on the reflectance spectra, the solar average absorptance of our silicone-hollow sphere sample and the commercial paint is calculated to be 0.20 and 0.26 respectively.

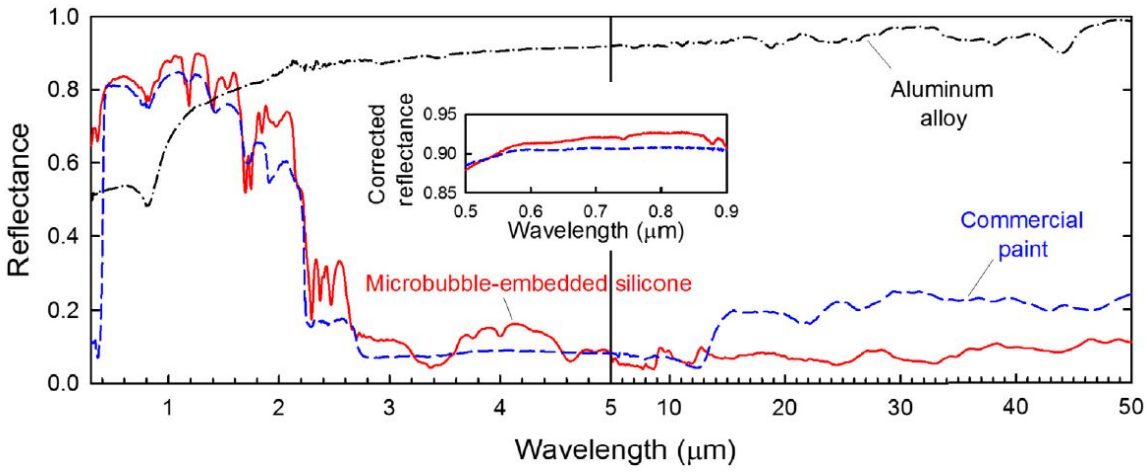

Figure 4.9. Reflectance spectrum of microbubble-embedded silicone (red solid line), commercial paint (blue dashed line), and 6061 aluminum alloy (black dash dotted line). The hollow microsphere-embedded silicon and commercial paint are coated on a black substrate. Inset shows the reflectance of the silicone measured using a single beam in an integrating sphere system after error correction.[†]

In mid-IR, our coating exhibits the highest emissivity ($1\text{-}R_0$) among the three compared samples over most of the spectrum $\lambda \geq 5\mu$m. We average the emissivity using the black-body radiation spectrum at T = 300 K as a weighting factor. The average emissivity of the microbubble-embedded silicone and the commercial paint is 0.93 and 0.78, respectively. As the temperature is lowered, the difference between the two emissivity values increases. For example, at T = 100 K, the average emissivity for the microbubble-embedded silicone and the commercial paint is 0.91 and 0.78, respectively. These values represents how much cooling can be achieved by mid-IR radiation when the surrounding environment is a black-body, e.g. the outer space. For terrestrial cooling applications, the emissivity over the atmospheric transparency window (8-13 μm) is important. The average emissivity over this window is 0.93 and 0.94 for both our sample

and the commercial paint. This similarity shows that the heat loss by mid-IR radiation is similar for two materials under terrestrial conditions, whereas our sample would perform better in the outer space. Nevertheless, our coating shows stronger solar rejection than the commercial paint and would perform better under both terrestrial and extra terrestrial conditions.

To improve the accuracy of reflectance measurements as shown in Fig. 4.9, we employed the error corrections to the measured reflectance. The correct R_0 spectra for our hollow microsphere in silicone sample (red solid line) and the commercial paint (blue dashed line) are shown in Fig. 4.9 inset. For our microbubble sample, the average reflectance, after the correction is made to the measurement by the Ocean Optics setup, is 0.92 over 0.5 μm $\leq \lambda \leq$ 0.9 μm, while it is 0.82 from the measurement by PerkinElmer setup. The error correction modifies the spectral dependence of the reflection. However, the error correction is not the source of a large difference in reflectance of 0.1 between the two setups. Even without the error correction, the average reflectance from the Ocean Optics setup is 0.92 ± 0.007, and the average reflectance of 0.92 remains almost unchanged by the correction.

While the origin of the difference in reflectance from the two setups is still under further investigation, both measurements consistently show that our microbubble in silicone sample has a higher reflectance than the commercial paint. For 2-mm-thick sample without a black coating, appreciable light transmission for our sample can be observed, while this transmission is absent for the commercial paint. From this observation and Fig. 4.9, we see that the commercial paint absorbs light significantly, which agrees with the simulation result in reference [112]. We also note that light

transmitted our microbubble film to a depth (≥ 2mm) comparable to the radius (4 mm) of the aperture of the Ocean Optics integrating sphere. This suggest that, in reflectance measurements with the integrating sphere, some diffuse photon flux of reflected light from the deep regions in the film cannot reach the sphere aperture, leading to an underestimation of the reflectance (same internal-diffused error in ref. [107]). Therefore, we speculate that the actual reflectance improvement of our hollow microsphere-silicone sample over the commercial paint would be even greater than previously shown.

An implication of our coating having higher reflectance in the solar spectrum is that, under the same solar radiation, the temperature rise in our sample will be smaller than that in the commercial paint. We've built a setup to test this hypothesis and the result is shown in Fig. 4.10. In the figure, the sample temperatures (T) relative to the ambient temperature (T_{amb}~20 °C), $\Delta T = T - T_{amb}$, is shown as a function of time (t) averaged over seven measurements. ΔT begins to rise when the solar simulator light is turned on at t = 8 min and reaches a plateau for our hollow microsphere-embedded silicone sample and the commercial paint sample by t = 46 min, when the light is turned off. The aluminum alloy does not reach a steady-state temperature by t = 46 min. After the light exposure ends, the temperatures decrease exponentially over time. From these data, the solar average absorptance, $\langle A \rangle$, can be calculated from a heat balance equation:

$$m\hat{C}_p \frac{d\Delta T}{dt} = T_{LDPE} S_b J \langle A \rangle - hS\Delta T - S\varepsilon\sigma(T^4 - T_{amb}^4), \tag{4-2}$$

where m is the sample mass, $\hat{C}_p$ is the specific heat capacity of each sample, T_{LDPE} is the transmittance of LDPE film of the box, S_b is the illumination area, J = 1000 W/m^2 is the solar radiation intensity, h is the heat transfer coefficient, ε is the mid-IR emissivity, σ is

Stefan-Boltzmann constant, and S is the surface area of the sample. In this equation, we assume that the sample surrounding is a mid-IR black body, and the temperature dependence of ε is negligible. At t = 46 min, the light is turned off, and J = 0 W/m^2. For the aluminum alloy, ε is less than 0.08, and thus the radiation term (containing ε) is also negligible. Therefore, the only heat conduction term remains and the solution for Eq. (4-2) for t > 46 min is

$$\ln\left(\frac{\Delta T_s}{\Delta T}\right) = \frac{hS}{m\hat{C}_p}(t - 46\,\text{min}), \tag{4-3}$$

where the subscript s denotes a state at t = 46 min. Eq. (4-3) is fit to the measured ΔT for the alloy. With $\hat{C}_p = 1.0 J/(g.K)$, [113] we obtain h = 8.2 W/(m^2.K). Then, $\langle A \rangle$'s for our microbubble sample and the commercial paint are calculated from the steady-state solution to Eq. (4-2),

$$\langle A \rangle = \frac{S}{T_{LDPE} S_b J}\left[h\Delta T_s + \varepsilon\sigma\left(T_s^4 - T_{amb}^4\right)\right]. \tag{4-4}$$

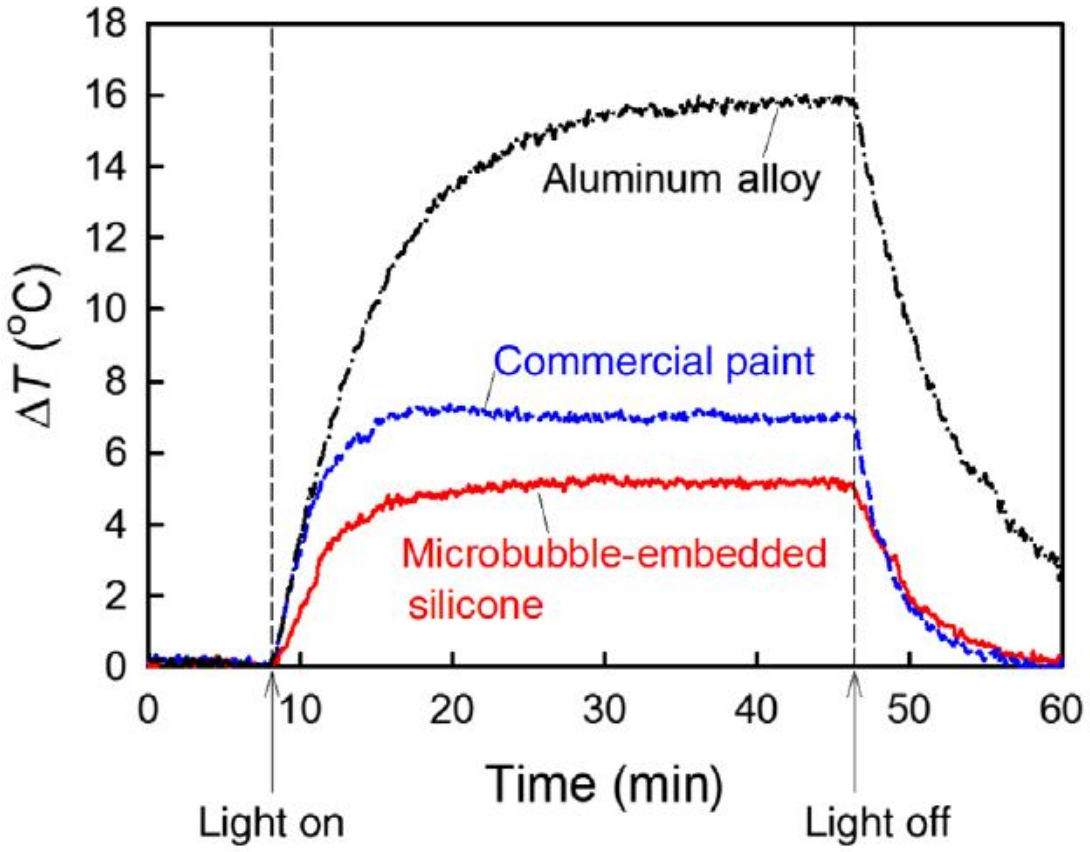

Figure 4.10. Temperature of a black substrate coated with microbubble-embedded silicon (red), a black substrate coated with commercial paint (blue) and 6061 aluminum alloy (black), relative to the ambient temperature. The samples are illuminated by a solar simulator beam of AM1.5G spectrum.[†]

Using the measured emissivity in Fig. 4.9, we find the $\langle A \rangle$ values to be 0.20 and 0.26 for the hollow microsphere sample and the commercial paint, respectively, from Eq. (4-4). These values are the same as those obtained by averaging the reflectance spectra in Fig. 4.9 using the AM1.5G intensity as a weighting factor. Because our microbubble coating has a lower $\langle A \rangle$ than the commercial paint by 0.06, employing our materials

instead of the commercial paint would increase the solar rejection power by as much as 0.06×1000 W/m^2 = 60 W/m^2.

The measured temperature variation over time from our outdoor experiment is shown in Fig. 4.11. During the time when the sunlight is intense, i.e., between 11 am to 4 pm, the average temperature of the substrate coated with our microbubble-embedded silicone is 1.3 °C below that of the substrate coated the commercial paint. This difference is slightly smaller than that during the experiment with the solar simulator (1.9 °C as shown in Fig. 4.10). This is because the average solar intensity during the sunlight exposure on the partly cloudy day is lower than the standard beam intensity of J = 1000 W/m^2. We note that increasing the thickness of our silicone coating would further decrease the substrate temperature under the solar radiation by reducing the light absorption by the black paint at the bottom of the sample. On the contrary, one cannot reduce the substrate temperature of the substrate further by increasing the thickness of the commercial paint beyond 2mm, because the sunlight is absorbed almost completely in the paint.

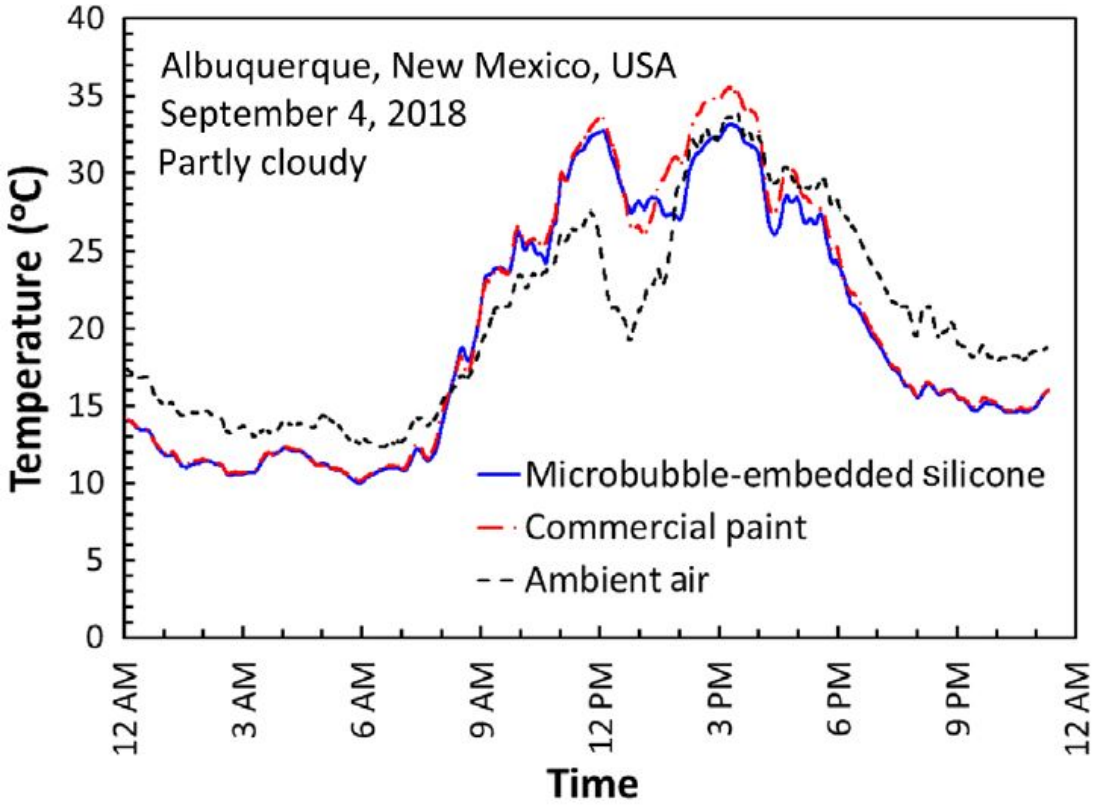

Figure 4.11. Measured temperature variation over a day for microbubble-embedded silicone sample (blue solid line), commercial paint (red dot-dashed line), and ambient air (black dash line).[†]

At night, the temperatures of both samples are below the ambient temperature by ~4 °C. This similarity shows that the cooling power due to mid-IR radiation through the atmospheric transparency window is nearly the same for two samples, which agrees with Fig. 4.9, where the emissivity values are similar within the window. Nevertheless, the solar scattering power is greater for our hollow microsphere-embedded silicone sample. Our sample temperature is higher than the ambient temperature between 8:15 am and 1:50 pm. After 1:50 pm, our sample temperature falls below the ambient temperature. This indicates that the heat loss through mid-IR radiation is stronger after 1:50 pm than that in the morning despite that the solar intensity at 1:50 pm is higher than in the

morning. This time variation in mid-IR heat loss is likely due to a change in the atmospheric transparency window.

4.5 Conclusion

We have demonstrated that the two types of white coatings, one based on hollow polymer microspheres and the other on the microspheres embedded in silicone, possess excellent radiative cooling properties under the sunlight. The coatings are fabricated with commercially available and inexpensive materials and low-cost processing steps. By using hollow microspheres instead of solid microspheres as in the previous work, the light scattering efficiency in the solar spectrum increases by around 100%. When embedding the hollow microspheres into silicone matrix, the resulting coating exhibits high mechanical durability and 6% less absorptance than that of commercial paint at the same thickness. Under the natural sunlight, the substrate coated with either of our coatings is cooler than that coated with commercial paint by ~2°C at most. For the microbubble-embedded silicone coating, the substrate temperature could be lowered further by simply increasing the coating thickness or by adjusting the size of the microspheres and fill fraction. Additionally, since silicone is a space-qualified stable material in outer space environments, our microbubble-embedded silicone coating could also be used for heat management in space. In this case, the radiative cooling would be even more improved from that in the terrestrial environment because the mid-IR radiation is no longer limited to the atmospheric transparency window.

Portions of this chapter have been published as J. D. Alden, S. Atiganyanun, R. Vanderburg, S. H. Lee, J. B. Plumley, O. K. Abudayyeh, S. M. Han, and S. E. Han, JPE **9**, 032705 (2019) and are reproduced with permission of the publisher.

[†]Figure reproduced with permission from J. D. Alden, S. Atiganyanun, R. Vanderburg, S. H. Lee, J. B. Plumley, O. K. Abudayyeh, S. M. Han, and S. E. Han, JPE **9**, 032705 (2019).

Chapter 5: Conclusion and Future Work

In this dissertation, we have explored the field of disordered photonics via microsphere-based structures. Two common themes shared among all the studies in this dissertation are the following. First, microspheres are versatile building blocks of disordered photonic structures and, by carefully investigating and systematically manipulating facile fabrication methods, we are able to control degrees of randomness in microsphere-based structures, which enable them to be used in photon management applications such as radiative cooling in this work. Second, the geometry of microspheres allows us to explore theoretical studies and build models to predict, describe, and understand the optical behaviors of our photonic media. By combining both the ease in fabrication of microsphere-based structures and the powerful theoretical approaches, the rich and useful phenomena associated with our disordered structures can be realized.

In the Langmuir-Blodgett work, we have demonstrated that structural randomness can be systematically introduced into microsphere-based photonic structures by carefully controlling assembly parameters, i.e. surface pressure and pulling speed. Our material balance consideration, supported by our experimental results, provides a guideline for maximizing the structural order. To controllably introduce randomness, the assembly approach is to begin from optimum pulling speed and surface pressure and then gradually increase the pulling speed while adjusting the surface pressure according to our quantitative model.

Following our findings in this Langmuir-Blodgett work, we can apply the fabrication method for mimicking biological photonic structures, since they incorporate

significant degree of randomness. Also in future work, optical properties, such as angle-dependent reflection, that result from the randomness in ordered structures could also be explored using our fabrication method. The model developed in this work could be extended to consider other geometric particles in addition to spheres and thus expand the versatility of the LB assembly in inducing randomness in many photonic structures. Langmuir Blodgett assembly is widely used for creating ordered structures in many non-photonic applications. By applying our model as a guide for introducing randomness, other interesting phenomena might be observed and be proven to be useful.

We also demonstrate one important application of disordered microsphere-based coating: radiative cooling. Our coatings are able to achieve excellent cooling performance without the use of expensive material or fabrication methods. This is accomplished by employing facile, scalable, low cost methods, colloidal sedimentation and spray coating. We also improve the mechanical durability of the microsphere-based coating by incorporating silicone matrix, which also renders our structures appropriate for outer space applications. A model developed in these works shows that the optical scattering power can be maximized with judicious choice of microsphere size, material and fill fraction. Importantly, the model shows that there is still much room for improvement in radiative cooling efficiency in the disordered structures. Our future works, following the model's prediction, will look into achieving even better radiative cooling performance while maintaining the facileness and the scalability.

Radiative cooling, while important on its own, is not the only application that can be achieved with microsphere-based structures. One particular usage that interests us is in ambient water harnessing. In this field, one can design a disordered structure that

incorporates both radiative cooling properties and surface energy engineering to enhance water collection from air. A collector cooled with radiative cooling would increase condensation rate of water vapor into droplets, while efficient design of surface energy profile in the collector would promote movement of droplets and thus enhance water collection rate. Improvement in ambient water harnessing technologies can have a significant impact, especially in developing countries where clean water is scarce.

Appendices

Appendix A: Verification of microsphere immersion at liquid surface

Here we validated the assumption that most of the microsphere volume is under the water surface. We consider a microsphere of radius R that has a surface tension Υ as shown in Fig. A1. The meniscus shape is described by $y = f(x)$ and becomes horizontal at a distance far from the microsphere. The meniscus forms a contact angle θ_c at the microsphere contact point. We consider a line that passes through the contact point and is tangent to the sphere and set the angle between the contact line and the y-axis to be α. The degree of microsphere immersion is measured by h, which us the distance between the microsphere center and the water surface in an absence of the microsphere. h is positive when more than a half of the microsphere volume is immersed in water.

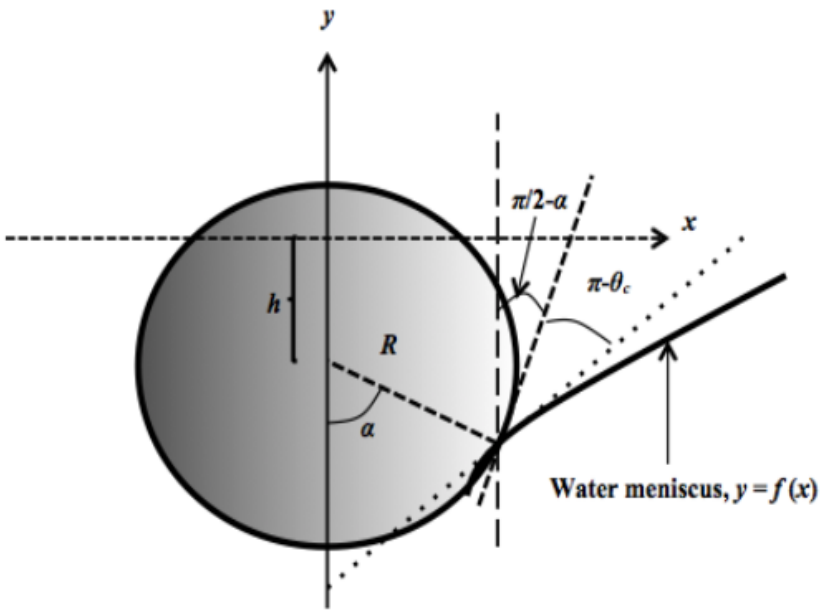

Figure A1. Schematic illustration of a microsphere at a water surface. †

The degree of immersion is determined by balance between surface tension, gravity, and buoyancy force. The *y*-direction components of these forces are denoted by f_s, f_g, and f_b, respectively. The expressions for these components are given by

$$f_s = 2\pi R\gamma \cdot \sin\alpha \cdot \cos\left(\frac{3\pi}{2} - \alpha - \theta_c\right) = -2\pi R\gamma \sin\alpha \sin(\alpha + \theta_c), \tag{A-1}$$

$$f_g = -\frac{4\pi}{3} R^3 \rho_s g, \tag{A-2}$$

$$f_b = \int_0^{\alpha} (P_s - P_a) 2\pi R^2 \cos\theta \sin\theta d\theta, \tag{A-3}$$

where ρ_s is the density of the microsphere, g is the acceleration of the gravity, P_a is the atmospheric pressure, and P_s is the pressure acting on the microsphere by the water. The difference in pressures, P_s - P_a, is equal to $\rho g(h + R\cos\theta)$, where ρ is the water density. Therefore, eq. (A-3) can be written as

$$f_b = \rho g(h + R\cos\theta) 2\pi R^2 \cos\theta \sin\theta d\theta = \frac{2\pi}{3} R^3 \rho g\left(1 + \frac{3h}{2R}\sin^2\alpha - \cos^3\alpha\right) \tag{A-4}$$

At equilibrium, the sum of all three components must be equal to zero

$$-2\pi R\gamma \sin\alpha \sin\left(\alpha + \theta_c\right) - \frac{4\pi}{3} R^3 \rho_s g + \frac{2\pi}{3} R^3 \rho g\left(1 + \frac{3h}{2R}\sin^2\alpha - \cos^3\alpha\right) = 0 \tag{A-5}$$

To express h in terms of α in Eq. (A-5), we invoke the Laplace-Young equation:

$$P - P_a = \gamma\left(\frac{1}{R_1} - \frac{1}{R_2}\right), \tag{A-6}$$

where P is the pressure inside the liquid at the meniscus, and R_1 and R_2 are the radii of the principal curvatures of the meniscus. Considering a curve that is the intersection of the

meniscus and the *xy*-plane, we see that the curvature of this curve ($1/R_1$) is much larger than that of a circle ($1/R_2$) on the meniscus centered at the *y*-axis. Therefore, we can approximate the pressure difference as

$$P - P_a = -\gamma \frac{y''}{\left(1+\left(y'\right)^2\right)^{3/2}}. \tag{A-7}$$

Further, we assume that $\left|y'\right| << 1$, which will be justified later. Because P-P_a is given by –ρ*gy*, eq. (A-6) can be written as

$$y'' = \frac{\rho g}{\gamma} y. \tag{A-8}$$

Integrating Eq. (A-8) with the boundary condition that $y' \to 0$ as $y \to 0$, we arrive at

$$y' = -\sqrt{\frac{\rho g}{\gamma}} y. \tag{A-9}$$

The assumption $\left|y'\right| << 1$ is justified from Eq. (A-9). In our experiment, *y* is of the order of a micron, ρ is 10^3 kg.m^{-3}, *g* is 9.8 m.s^{-2}, and γ is 0.072 J.m^{-2}. Accordingly, y' is of the order of 10^{-4}, which is significantly smaller than 1.

At the meniscus-microsphere contact point, $y' = -\tan(\alpha + \theta_c)$ and $y = -(h + R\cos\theta)$. Thus, Eq. (A-9) becomes

$$\tan(\alpha + \theta_c) = -\sqrt{\frac{\rho g}{\gamma}} (h + R\cos\theta). \tag{A-10}$$

Using this equation to eliminate h is Eq. (A-5), we have

$$\frac{\gamma}{\rho g R^2}\sin\alpha\sin\left(\alpha+\theta_c\right)+\frac{1}{2}\sqrt{\frac{\gamma}{\rho g R^2}}\tan(\alpha+\theta_c)\sin^2\alpha-\frac{1}{3} \\ +\frac{1}{2}\cos\alpha-\frac{1}{6}\cos^3\alpha+\frac{2}{3}\frac{\rho_s}{\rho}=0 \quad \text{(A-11)}$$

In our system, $\sqrt{\frac{\gamma}{\rho g R^2}}$ is approximately 6000, and thus the first term dominates the other terms in Eq. (A-11). This happens when α is not very close to 0 or π, which corresponds to a very hydrophobic (or very hydrophilic surface). With these approximations, Eq. (A-11) can be ultimately simplified to

$$\alpha+\theta_c=\pi\,. \quad \text{(A-12)}$$

Because $\frac{\gamma}{\rho g R}\sin(\alpha+\theta_c)$ in Eq. (A-11) should be of the order of 1 for the first term to be comparable to the other terms, $\sqrt{\frac{\gamma}{\rho g R^2}}\tan(\alpha+\theta_c)$ is much less than 1. This means that eq. Eq. (A-10) becomes

$$\frac{h}{R}=-\sqrt{\frac{\gamma}{\rho g R^2}}\tan(\alpha+\theta_c)-\cos\alpha\cong-\cos\alpha=\cos\theta_c\,, \quad \text{(A-13)}$$

where the last equality is from Eq. (A-12). Therefore, the degree of microsphere submersion is approximately a function of only the contact angle and the microsphere radius.

To determine the degree of the submersion we measure the contact angle on a silica surface that is functionalized with allytrimethoxysilane similar to our microspheres. Specifically, we functionalize a glass slide and measure its contact angle to 47 degrees. From Eq. (A-13) and the measured contact angle, the sphere immersion distance, *h*, is

307 nm for our microspheres of radius 450 nm. This means that 84% of the microsphere is under the water surface.

So far, we have considered the case of a single microsphere at the water surface. In our experiment, multiple microspheres are close to one another. Nevertheless, Eq. (A-13) is still valid in this case. To see so, we consider the vertical distance between the contact point and the water level (y=0 surface) for the case of a single microsphere. This distance, which is $h + R\cos\alpha$ (note the negative cosine value), is calculated to be 0.1 nm only. For closely packed microspheres, consider two microspheres in contact with each other. The distance between the two points of the lowest meniscus (each point from each sphere) is given by $2R(1-\sin\alpha) = 242$ nm. This distance is much larger than the vertical distance of 0.1 nm. This implies that the meniscus near a microsphere is essentially flat and negligibly affected by the presence of surrounding microspheres. Therefore, for closely packed microspheres at the water surface, Eq. (A-13) is still applicable, and thus our assumption that most of the microsphere volume is under the water level is verified.

Portions of this chapter have been published as S. Atiganyanun, M. Zhou, O. K. Abudayyeh, S. M. Han, and S. E. Han, Langmuir **33**, 13783 (2017) and are reproduced with permission of the publisher.

[†]Figure reproduced with permission from S. Atiganyanun, M. Zhou, O. K. Abudayyeh, S. M. Han, and S. E. Han, Langmuir **33**, 13783 (2017).

Appendix B: Error corrections in the measurement of reflectance.

For error corrections in the integrating sphere measure of reflectance R_0, we consider the following model. f_d is defined as the ratio of diffuse light power exiting out of an integrating sphere to the preceding coming into the integrating sphere. When a sample film of reflectance R_0 is placed on top of the open port of the integrating sphere, the power measured by the detector connected to the sphere is

$$P_m = C(R_0 + f_d R_0^2 + f_d^2 R_0^3 + ...) = C\frac{R_0}{1 - f_d R_0}, \tag{A-14}$$

where C is a constant. When a silver (Ag) film is placed at the port, the detected power is the same as Eq. (A-14) with R_0 being replaced by the silver reflectance R_{Ag}. The measured reflectance of the sample film R_m is the ratio of the power between the two cases so that

$$R_m = \frac{R_0(1 - f_d R_{Ag})}{R_{Ag}(1 - f_d R_0)}. \tag{A-15}$$

To obtain R_0 from Eq. (A-15), we need to determine f_d.

To find f_d, we consider an experiment where a Lambertian scattering white film is located above the integrating sphere with a separation distance δ as shown in Fig. A2. inset. We define the following fraction:

f_0 = ratio of diffuse light power entering into an integrating sphere to that precedingly scattered downward from the white film.

f_1 = ratio of diffuse light power entering into an integrating sphere by being reflected from a white film to that precedingly exiting out of an integrating sphere.

When transmittance of the film is T_0, the transmittance T_m measured from the light power collected through the detector port in the integrating sphere is

$$T_m(\delta) = \frac{T_0 f_0(\delta)}{1 - f_1(\delta) f_d} . \tag{A-16}$$

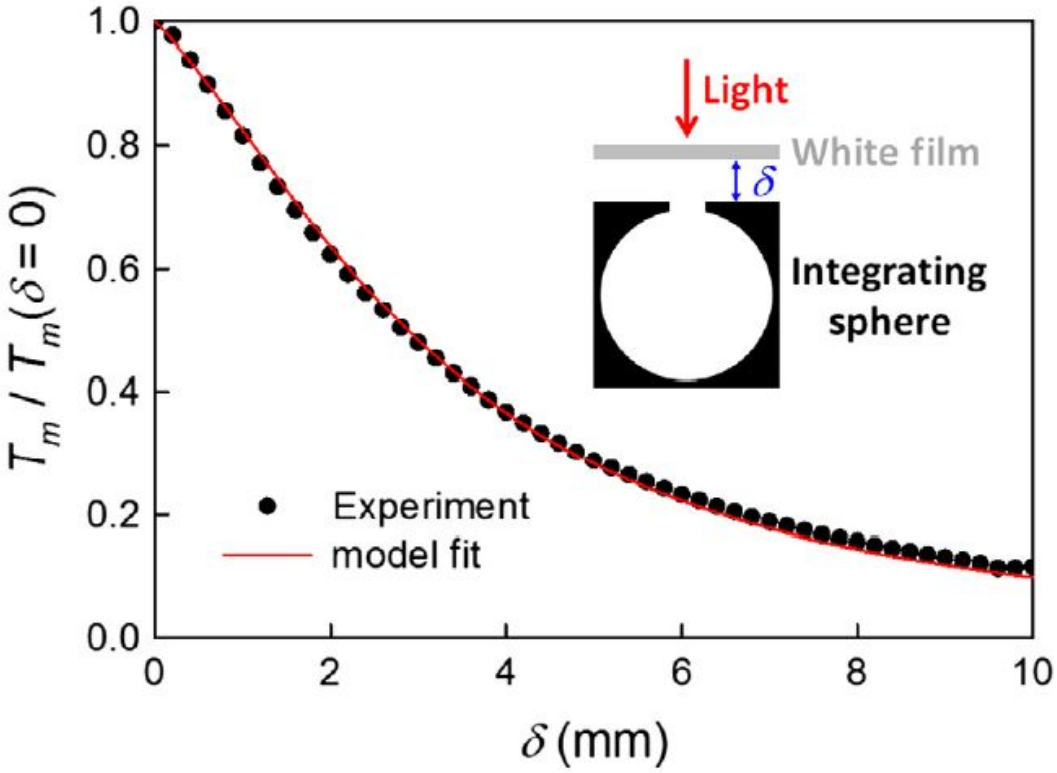

Figure A2. Dependence of normalized transmittance on the distance δ between the white film and the inlet of our integrating sphere obtained from experiment (black circle) and model fit (red line). †

Because $f_0 = 1$ and $f_1 = R_0$ at $\delta = 0$, Eq. (A-16) can be also expressed as

$$\frac{T_m(\delta)}{T_m(0)} = \frac{(1-R_0 f_d) f_0(\delta)}{1-f_1(\delta) f_d}. \tag{A-17}$$

We experimentally determined that the incident light intensity has a Gaussian profile with a beam width of 2σ = 1.91 mm at λ = 650 nm. In this case, we obtain f_0 as

$$f_0 = \frac{1}{2\pi\sigma^2} \int_0^R \int_0^{2\pi} \rho \exp(-\frac{\rho^2}{2\sigma^2}) \sin^2\theta_m d\varphi d\rho, \tag{A-18}$$

where $\tan\theta_m = \left(\sqrt{R^2 - \rho^2 \sin^2\varphi} - \rho\cos\varphi\right)/\delta$ with R being the radius of the light-inlet port of the integrating sphere. We also find an expression for f_1 as

$$f_1 = \frac{R_0}{\pi^2 R^2} \int_0^R \int_0^{2\pi} \int_0^{\pi/2} \int_{|\sin\varphi_2| \le R/\rho_2} \rho_1 \left(\sin^2\theta_{2,\max} - \sin^2\theta_{2,\min}\right) \cos\theta_1 \sin\theta_1 d\varphi_2 d\theta_1 d\varphi_1 d\rho_1, \tag{A-19}$$

where $\tan\theta_{2,\max} = \left(\sqrt{R^2 - {\rho_2}^2 \sin^2\varphi_2} - \rho_2\cos\varphi_2\right)/\delta$,

$\tan\theta_{2,\min} = \left(-\sqrt{R^2 - \rho_2^2 \sin^2\varphi_2} - \rho_2\cos\varphi_2\right)/\delta$, and

$\rho_2 = \sqrt{\rho_1^2 + \delta^2 \tan^2\theta_1 + 2\rho_1\delta\tan\theta_1\cos\varphi_1}$. To find f_d, we experimentally measured $T_m(\delta)$ and fit $T_m(\delta)/ T_m(0)$ to Eq. (A-17) as shown in Fig. 5. For the fitting, R_0 is approximated by R_m. With coefficient of determination of 0.999 for the fitting, we obtain f_d = 0.312 for the integrating sphere. Using this value of f_d, we solve Eq. (A-15) for R_0.

Portions of this chapter have been published as J. D. Alden, S. Atiganyanun, R. Vanderburg, S. H. Lee, J. B. Plumley, O. K. Abudayyeh, S. M. Han, and S. E. Han, JPE **9**, 032705 (2019) and are reproduced with permission of the publisher.

[†]Figure reproduced with permission from J. D. Alden, S. Atiganyanun, R. Vanderburg, S. H. Lee, J. B. Plumley, O. K. Abudayyeh, S. M. Han, and S. E. Han, JPE **9**, 032705 (2019).

References

[1] E. Yablonovitch, Phys. Rev. Lett. **58**, 2059 (1987).

[2] S. John, Phys. Rev. Lett. **58**, 2486 (1987).

[3] Y. A. Vlasov, X. Z. Bo, J. C. Sturm, D. J. Norris, S. P. 194021 Ioffe Phys Tech Inst, D. E. E. Princeton Univ, and C. P. & O. M. Princeton Univ, Nature **414**, 289 (2001).

[4] S. Noda, A. Chutinan, and M. Imada, Nature **407**, 608 (2000).

[5] A. Blanco, E. Chomski, S. Grabtchak, M. Ibisate, S. John, S. W. Leonard, C. Lopez, F. Meseguer, H. Miguez, J. P. Mondia, G. A. Ozin, O. Toader, and H. M. van Driel, Nature **405**, 437 (2000).

[6] S. E. Han, A. Stein, and D. J. Norris, Phys. Rev. Lett. **99**, 053906 (2007).

[7] S. E. Han, Phys. Rev. B **80**, 155108 (2009).

[8] J. B. Chou, Y. X. Yeng, Y. E. Lee, A. Lenert, V. Rinnerbauer, I. Celanovic, M. Soljačić, N. X. Fang, E. N. Wang, and S.-G. Kim, Adv. Mater. **26**, 8041 (2014).

[9] S. Noda, M. Fujita, and T. Asano, Nat. Photonics **1**, 449 (2007).

[10] P. Bermel, C. Luo, L. Zeng, L. C. Kimerling, and J. D. Joannopoulos, Opt. Express **15**, 16986 (2007).

[11] S. H. Fan, P. R. Villeneuve, J. D. Joannopoulos, and E. F. Schubert, Phys. Rev. Lett. **78**, 3294 (1997).

[12] S. Nishimura, N. Abrams, B. A. Lewis, L. I. Halaoui, T. E. Mallouk, K. D. Benkstein, J. van de Lagemaat, and A. J. Frank, J. Am. Chem. Soc. **125**, 6306 (2003).

[13] J. D. Joannopoulos, S. G. Johnson, J. N. Winn, and R. D. Meade, *Photonic Crystals: Molding the Flow of Light* (2008).

[14] O. Painter, R. K. Lee, A. Scherer, A. Yariv, J. D. O'Brien, P. D. Dapkus, and I. Kim, Science **284**, 1819 (1999).

[15] J. C. Knight, T. A. Birks, P. S. Russell, and D. M. Atkin, Opt. Lett. **21**, 1547 (1996).

[16] J. C. Knight, J. Broeng, T. A. Birks, and P. S. J. Russel, Science **282**, 1476 (1998).

[17] J. S. Foresi, P. R. Villeneuve, J. Ferrera, E. R. Thoen, G. Steinmeyer, S. Fan, J. D. Joannopoulos, L. C. Kimerling, H. I. Smith, and E. P. Ippen, Nature **390**, 143 (1997).

[18] A. Mekis, J. C. Chen, I. Kurland, S. H. Fan, P. R. Villeneuve, and J. D. Joannopoulos, Phys. Rev. Lett. **77**, 3787 (1996).

[19] H. M. Whitney, M. Kolle, P. Andrew, L. Chittka, U. Steiner, and B. J. Glover, Science **323**, 130 (2009).

[20] P. Vukusic and J. R. Sambles, Nature **424**, 852 (2003).

[21] S. Kinoshita and S. Yoshioka, ChemPhysChem **6**, 1442 (2005).

[22] S. Kinoshita, S. Yoshioka, and J. Miyazaki, Rep. Prog. Phys. **71**, 076401 (2008).

[23] D. S. Wiersma, Nat. Photonics **7**, 188 (2013).

[24] Y. Zhao, Z. Xie, H. Gu, C. Zhu, and Z. Gu, Chem. Soc. Rev. **41**, 3297 (2012).

[25] Vukusic P., Sambles J. R., Lawrence C. R., and Wootton R. J., Proceedings of the Royal Society of London. Series B: Biological Sciences **266**, 1403 (1999).

[26] Kinoshita Shuichi, Yoshioka Shinya, and Kawagoe Kenji, Proceedings of the Royal Society of London. Series B: Biological Sciences **269**, 1417 (2002).

[27] D. W. Lee, American Scientist **85**, 56 (1997).

[28] D. E. McCoy, T. Feo, T. A. Harvey, and R. O. Prum, Nature Communications **9**, 1 (2018).

[29] K. Vynck, M. Burresi, F. Riboli, and D. S. Wiersma, Nature Materials **11**, 1017 (2012).

[30] V. E. Ferry, M. A. Verschuuren, M. C. van Lare, R. E. I. Schropp, H. A. Atwater, and A. Polman, Nano Lett. **11**, 4239 (2011).

[31] E. R. Martins, J. Li, Y. Liu, V. Depauw, Z. Chen, J. Zhou, and T. F. Krauss, Nature Communications **4**, 2665 (2013).

[32] S. Ghosh, and B. R. Hoard, E. C. Culler, J. E. Bonilla, E. J. Martin, J. Grey, S. M. Han, and S. E. Han, in *2015 IEEE 42nd Photovoltaic Specialist Conference (PVSC)* (2015), pp. 1–3.

[33] S. J. Han, S. Ghosh, O. K. Abudayyeh, B. R. Hoard, E. C. Culler, J. E. Bonilla, S. M. Han, and S. E. Han, Opt Express **24**, A1586 (2016).

[34] M. D. Kelzenberg, S. W. Boettcher, J. A. Petykiewicz, D. B. Turner-Evans, M. C. Putnam, E. L. Warren, J. M. Spurgeon, R. M. Briggs, N. S. Lewis, and H. A. Atwater, Nature Materials **9**, 239 (2010).

[35] J. Topolancik, B. Ilic, and F. Vollmer, Phys. Rev. Lett. **99**, 253901 (2007).

[36] M. Notomi, H. Suzuki, T. Tamamura, and K. Edagawa, Phys. Rev. Lett. **92**, 123906 (2004).

[37] N. Vogel, R. A. Belisle, B. Hatton, T.-S. Wong, and J. Aizenberg, Nat Commun **4**, 2167 (2013).

[38] K. E. Jensen, D. Pennachio, D. Recht, D. A. Weitz, and F. Spaepen, Soft Matter **9**, 320 (2012).

[39] D. J. Norris, E. G. Arlinghaus, L. Meng, R. Heiny, and L. E. Scriven, Advanced Materials **16**, 1393 (2004).

[40] P. Jiang, J. F. Bertone, K. S. Hwang, and V. L. Colvin, Chem. Mater. **11**, 2132 (1999).

[41] J. E. G. J. Wijnhoven and W. L. Vos, Science **281**, 802 (1998).

[42] M. Bardosova, M. E. Pemble, I. M. Povey, and R. H. Tredgold, Advanced Materials **22**, 3104 (2010).

[43] S. Reculusa, R. Perrier-Cornet, B. Agricole, V. Héroguez, T. Buffeteau, and S. Ravaine, Phys. Chem. Chem. Phys. **9**, 6385 (2007).

[44] B. van Duffel, R. H. A. Ras, F. C. D. Schryver, and R. A. Schoonheydt, J. Mater. Chem. **11**, 3333 (2001).

[45] M. Szekeres, O. Kamalin, R. A. Schoonheydt, K. Wostyn, K. Clays, A. Persoons, and I. Dékány, J. Mater. Chem. **12**, 3268 (2002).

[46] P. D. García, R. Sapienza, Á. Blanco, and C. López, Adv. Mater. **19**, 2597 (2007).

[47] P. M. Piechulla, L. Muehlenbein, R. B. Wehrspohn, S. Nanz, A. Abass, C. Rockstuhl, and A. Sprafke, Advanced Optical Materials **6**, 1701272 (2018).

[48] R. Fenollosa, F. Meseguer, and M. Tymczenko, Advanced Materials **20**, 95 (2008).

[49] S. A. Kalogirou, Progress in Energy and Combustion Science **30**, 231 (2004).

[50] C. Tzivanidis, E. Bellos, D. Korres, K. A. Antonopoulos, and G. Mitsopoulos, Case Studies in Thermal Engineering **6**, 226 (2015).

[51] U.S. Energy Information Administration, Office of Energy Consumption and Efficiency Statistics, Table HC7.1 Air Conditioning in U.S. Homes by Housing Unit Type, 2015 (2015).

[52] U.S. Energy Information Administration (EIA), 2009 RECS Survey Data (2013).

[53] D&R International, Ltd (U.S. Department of Energy), *2011 Buildings Energy Data Book* (2012), p. 286.

[54] F. Trombe, Comptes Rendus de l'Académie Des Sciences **256**, 2013 (1963).

[55] F. Trombe, A. Le Phat Vinh, and M. Le Phat Vinh, J. Rech. CNRS **65**, 563 (1964).

[56] F. Trombe, A. Le Phat Vinh, and M. Le Phat Vinh, Comptes Rendus de l'Académie Des Sciences **258**, 5685 (1964).

[57] A. P. Raman, M. A. Anoma, L. Zhu, E. Rephaeli, and S. Fan, Nature **515**, 540 (2014).

[58] A. R. Gentle and G. B. Smith, Adv. Sci. **2**, 1500119 (2015).

[59] Y. Zhai, Y. Ma, S. N. David, D. Zhao, R. Lou, G. Tan, R. Yang, and X. Yin, Science **355**, 1062 (2017).

[60] J. Kou, Z. Jurado, Z. Chen, S. Fan, and A. J. Minnich, ACS Photonics **4**, 626 (2017).

[61] M. Bardosova, P. Hodge, L. Pach, M. E. Pemble, V. Smatko, R. H. Tredgold, and D. Whitehead, Thin Solid Films **437**, 276 (2003).

[62] M. Bardosova, M. E. Pemble, I. M. Povey, R. H. Tredgold, and D. E. Whitehead, Appl. Phys. Lett. **89**, 093116 (2006).

[63] A. Gil and F. Guitián, Journal of Colloid and Interface Science **307**, 304 (2007).

[64] S. Reculusa and S. Ravaine, Chem. Mater. **15**, 598 (2003).

[65] S. Reculusa and S. Ravaine, Applied Surface Science **246**, 409 (2005).

[66] J. Hur and Y.-Y. Won, Soft Matter **4**, 1261 (2008).

[67] A. S. Dimitrov and K. Nagayama, Langmuir **12**, 1303 (1996).

[68] B. E. Warren, *X-Ray Diffraction* (Courier Corporation, 1990).

[69] P.-S. Tsai, Y.-M. Yang, and Y.-L. Lee, Langmuir **22**, 5660 (2006).

[70] G. Tolnai, A. Agod, M. Kabai-Faix, A. L. Kovács, J. J. Ramsden, and Z. Hórvölgyi, J. Phys. Chem. B **107**, 11109 (2003).

[71] K. Muramatsu, M. Takahashi, K. Tajima, and K. Kobayashi, Journal of Colloid and Interface Science **242**, 127 (2001).

[72] C. G. Granqvist and A. Hjortsberg, Journal of Applied Physics **52**, 4205 (1981).

[73] C. S. Wojtysiak, US7503971 B2 (17 March 2009).

[74] B. (National I. of C. Orel, M. K. Gunde, and A. Krainer, Solar Energy (USA) (1993).

[75] A. W. Harrison and M. R. Walton, Solar Energy **20**, 185 (1978).

[76] M. Muselli, Energy and Buildings **42**, 945 (2010).

[77] A. Synnefa, M. Santamouris, and I. Livada, Solar Energy **80**, 968 (2006).

[78] R. F. Brady and L. V. Wake, Progress in Organic Coatings **20**, 1 (1992).

[79] R. Levinson, P. Berdahl, and H. Akbari, Solar Energy Materials and Solar Cells **89**, 351 (2005).

[80] B. Giera, L. A. Zepeda-Ruiz, A. J. Pascall, and T. H. Weisgraber, Langmuir **33**, 652 (2017).

[81] K. L. Wu and S. K. Lai, Langmuir **21**, 3238 (2005).

[82] E. J. Lavernia and Y. Wu, *Wiley: Spray Atomization and Deposition* (1997).

[83] V. Scardaci, R. Coull, P. E. Lyons, D. Rickard, and J. N. Coleman, Small **7**, 2621 (2011).

[84] R. H. Fernando, L.-L. Xing, and J. E. Glass, Progress in Organic Coatings **40**, 35 (2000).

[85] L.-L. Xing, J. E. Glass, and R. H. Fernando, in *Technology for Waterborne Coatings* (American Chemical Society, 1997), pp. 265–295.

[86] S. L. Shinde and G. S. Tendolkar, Powder Metallurgy International **9**, 180 (1977).

[87] M. A. Weiss, ARS Journal **29**, 252 (1959).

[88] A. Ishimaru, editor , in *Wave Propagation and Scattering in Random Media* (Academic Press, 1978), p. xiii.

[89] J. X. Zhu, D. J. Pine, and D. A. Weitz, Phys. Rev. A **44**, 3948 (1991).

[90] D. J. Durian, Phys. Rev. E **50**, 857 (1994).

[91] D. Contini, F. Martelli, and G. Zaccanti, Appl. Opt., AO **36**, 4587 (1997).

[92] K. Busch, C. M. Soukoulis, and E. N. Economou, Phys. Rev. B **50**, 93 (1994).

[93] C. M. Soukoulis, S. Datta, and E. N. Economou, Phys. Rev. B **49**, 3800 (1994).

[94] P. Kubelka, J. Opt. Soc. Am., JOSA **38**, 448 (1948).

[95] M. K. Gunde and Z. C. Orel, Appl. Opt., AO **39**, 622 (2000).

[96] H. C. Hottel, A. F. Sarofim, W. H. Dalzell, and I. A. Vasalos, AIAA Journal **9**, 1895 (1971).

[97] M. Q. Brewster and C. L. Tien, J Heat Transfer Trans ASME **V 104**, 573 (1982).

[98] G. Y. Onoda and E. G. Liniger, Phys. Rev. Lett. **64**, 2727 (1990).

[99] P. D. García, R. Sapienza, J. Bertolotti, M. D. Martín, Á. Blanco, A. Altube, L. Viña, D. S. Wiersma, and C. López, Phys. Rev. A **78**, 023823 (2008).

[100] W. L. Vos, T. W. Tukker, A. P. Mosk, A. Lagendijk, and W. L. IJzerman, Appl. Opt., AO **52**, 2602 (2013).

[101] W. Poon, E. R. Weeks, and C. P. Royall, Soft Matter **8**, 21 (2012).

[102] C. F. Bohren and D. R. Huffman, in *Absorption and Scattering of Light by Small Particles* (Wiley-VCH Verlag GmbH, 1998), pp. 57–81.

[103] M. M. Hossain and M. Gu, Adv Sci (Weinh) **3**, 1500360 (2016).

[104] H. C. deGroh, C. C. Daniels, J. A. Dever, S. K. Miller, D. L. Waters, J. R. Finkbeiner, P. H. Dunlap, and B. M. Steinetz, NASA/TM-2010-216332 E (2010).

[105] J. D. Alden, S. Atiganyanun, R. Vanderburg, S. H. Lee, J. B. Plumley, O. K. Abudayyeh, S. M. Han, and S. E. Han, JPE **9**, 032705 (2019).

[106] F. Hendriks and A. Aviram, Review of Scientific Instruments **53**, 75 (1982).

[107] F. J. J. Clarke and J. A. Compton, Color Research & Application **11**, 253 (1986).

[108] L. M. Hanssen, Appl. Opt., AO **35**, 3597 (1996).

[109] D. I. Milburn and K. G. T. Hollands, Solar Energy **55**, 85 (1995).

[110] R. D. Beauchemin, D. M. Wilt, and P. E. Hausgen, in *2017 IEEE 44th Photovoltaic Specialist Conference (PVSC)* (2017), pp. 102–106.

[111] D. M. Wilt, US8974899B1 (10 March 2015).

[112] M. A. Gali, A. R. Gentle, M. D. Arnold, and G. B. Smith, Appl. Opt., AO **56**, 8699 (2017).

[113] J. G. Michopoulos, A. Birnbaum, and A. P. Iliopoulos, V01AT02A017 (2016).